Scientific Basis and Initial Evaluation of the CLAVR-1 Global Clear/Cloud Classification Algorithm for the Advanced Very High Resolution Radiometer

LARRY L. STOWE, PAUL A. DAVIS, AND E. PAUL MCCLAIN

Office of Research and Applications, NOAA/NESDIS, Washington, D.C.

(Manuscript received 29 July 1996, in final form 22 May 1998)

ABSTRACT

An algorithm for the remote sensing of global cloud cover using multispectral radiance measurements from the Advanced Very High Resolution Radiometer (AVHRR) on board National Oceanic and Atmospheric Administration (NOAA) polar-orbiting satellites has been developed. The CLAVR-1 (Clouds from AVHRR-Phase I) algorithm classifies 2 × 2 pixel arrays from the Global Area Coverage (GAC) 4-km-resolution archived database into CLEAR, MIXED, and CLOUDY categories. The algorithm uses a sequence of multispectral contrast, spectral, and spatial signature threshold tests to perform the classification. The various tests and the derivation of their thresholds are presented. CLAVR-1 has evolved through experience in applying it to real-time *NOAA-11* data, and retrospectively through the NOAA AVHRR Pathfinder Atmosphere project, where 16 years of data have been reprocessed into cloud, radiation budget, and aerosol climatologies. The classifications are evaluated regionally with image analysis, and it is concluded that the algorithm does well at classifying perfectly clear pixel arrays, except at high latitudes in their winter seasons. It also has difficulties with classifications over some desert and mountainous regions and when viewing regions of ocean specular reflection. Generally, the CLAVR-1 fractional cloud amounts, when computed using a statistically equivalent spatial coherence method, agree to within about 0.05–0.10 of image/analyst estimates on average. There is a tendency for CLAVR-1 to underestimate cloud amount when it is large and to overestimate it when small.

1. Introduction

As numerical weather prediction and climate models become more sophisticated, they demand more accurate observations of atmospheric variables in order to validate the modeling of physical processes, as well as to assign initial values to the cloud parameters (Slingo 1990; Schiffer and Rossow 1983). The lack of accurate cloud physical processes in climate models is currently thought to be the major source of uncertainty in the prediction of climate change due to the ''greenhouse'' effect (Cess et al. 1989). Therefore, accurate remote sensing of cloud parameters is essential to the improvement of predictive model accuracies, as well as for monitoring climate change.

As an example, if the earth is about 50% cloud covered, as has been observed from *Nimbus-7* (Stowe et al. 1989), and if the seasonally and globally averaged cloud radiative effect is to cool the earth by about 25 W m^{-2}, (Ardanuy et al. 1991), a 0.01 change in fractional cloud cover with no change in cloud properties would change the cloud radiative effect by about 0.5 W m^{-2}. As doubling the amount of CO_2 gas in the atmosphere would heat the earth–atmosphere system by about 4 W m^{-2}, this could be compensated by an increase in cloud amount of about 0.08, a negative feedback effect of clouds. If cloud amount decreased as a consequence of the doubling of CO_2, at this time equally plausible, then the earth would heat by an additional 1 W m^{-2} for every 0.02 decrease in cloud amount, a positive feedback. Therefore, accuracy in cloud amount is important.

The National Oceanic and Atmospheric Administration (NOAA) has developed a cloud remote-sensing capability using Advanced Very High Resolution Radiometer (AVHRR) and TIROS Operational Vertical Sounder (TOVS) High-Resolution Infrared Sounder and Microwave Sounding Unit measurements that could satisfy these weather and climate applications (Stowe 1991) because 1) older cloud remote sensing programs such as International Satellite Cloud Climatology Project (ISCCP, Rossow et al. 1993) or Real-Time Nephanalysis (RTNEPH, Hamill et al. 1992) are restricted to only two of the many available channels from the NOAA Polar Orbiting Environmental Satellites (POES) instruments, limiting their ability to detect cirrus and low stratus clouds and to describe cloud properties over certain surface types, such as polar snow and ice, or to account for particle size effects on the retrieved cloud optical properties; and 2) these other programs do not provide for the computation of cloud amount from par-

Corresponding author address: Dr. Larry L. Stowe, Office of Research and Applications, NOAA/NESDIS, Washington, DC 20233.

tially cloud-filled pixels. These limitations can be overcome with multispectral approaches based on the physical discrimination features that separate clouds from background earth scenes. Examples of these approaches can be found in the literature, but none has been developed for global applications both day and night (e.g., Coakley and Bretherton 1982; Saunders and Kriebel 1988; Welch et al. 1988; Baum et al. 1992; Gutman 1992; Uddstrom and Gray 1996). Additionally, datasets such as the International Satellite Cloud Climatology Project (ISCCP) are retrospective (nonreal time) and climatological (sampled datasets averaged over large spatial areas) in design and cannot therefore meet the demands by the National Weather Service and NOAA's National Environmental Satellite Data and Information Systems (NESDIS) for near-real-time cloud products with high spatial resolution. Working in real time, the method described here has the potential of favorably impacting the quality of other climate-related products being produced at NESDIS [e.g., sea surface temperature (McClain et al. 1985), aerosol optical thickness (Stowe et al. 1997), and vegetation index (Tarpley et al. 1984)] by providing cloud screening information for the acquisition of clear-sky pixels. Tests are underway to evaluate the usefulness of CLAVR-1 (Clouds from AVHRR-Phase I) as a ''front-end'' processor and CLEAR/CLOUD classifier in the generation of NESDIS products.

In this article, the CLAVR-1 global CLEAR/CLOUD classification algorithm and its evaluation are described more fully than previously (Stowe et al. 1991; Hou et al. 1993; Stowe et al. 1995). It is the initial step in remote sensing of global cloud cover using multispectral radiance measurements from the AVHRR on board NOAA polar-orbiting satellites. The objectives of the CLAVR-1 algorithm are operational real-time processing to classify each 2 $\times$ 2 GAC pixel array (adjacent pixels on adjacent scan lines) as CLOUDY, MIXED, or CLEAR and to map total cloud amount on a global grid. A second-generation algorithm, CLAVR-2, has been developed at the pixel level to provide estimates of cloud cover by cloud type and layer. This major modification to the CLAVR-1 algorithm was needed to provide estimates of cloudiness in multiple atmospheric layers, as required by the weather and climate prediction communities (Rossow et al. 1993; Mokhov and Schlesinger 1993, 1994; Wylie et al. 1994). The multiple-layer cloud analysis (MLCA) algorithm is described and validated in two papers currently in preparation for submission to this journal (Davis et al. 1999, manuscript submitted to *J. Atmos. Oceanic Technol.*, Luo et al. 1999, manuscript submitted to *J. Atmos. Oceanic Technol.*). A third-generation algorithm, CLAVR-3, uses predicted cloud/no-cloud thresholds from an analysis of previously sampled clear-sky radiance statistics (Stowe et al. 1993) to increase the quantity while maintaining the quality of individual CLEAR pixels by reclassifying 2 $\times$ 2 pixel arrays that were considered ambiguous in CLAVR-1. This algorithm is described in a companion paper (Vemury et al. 1999, manuscript submitted to *J. Atmos. Oceanic Technol.*), which contains additional evaluation tests to further verify the quality of the CLEAR classifications from CLAVR-1 and 3.

The scientific basis of cloud detection with multispectral imager data is given in section 2. Application of these basics to global AVHRR data is discussed in section 3, and section 4 describes the cloud test sequencing and treatment of ambiguities. Qualitative and quantitative regional evaluations of the algorithm follow in section 5, and discussion and concluding remarks are presented in section 6. Comprehensive decision-tree flowcharts are presented in the appendix, together with details of the derivation of some of the tests, their associated thresholds, and other related matters.

2. Bases of cloud detection with multispectral imager data

Before describing the CLAVR-1 daytime and nighttime cloud classification algorithms in section 3 and the appendix, the basis from which the earth's clouds can be detected with multispectral imagery (i.e., contrast, spectral, and spatial signatures) is briefly discussed. A multispectral imager provides measurements of the radiance (energy/area/solid angle/spectral interval) for each discrete element of the image (pixel). These radiances can be described with radiative transfer theory. In the solar part of the spectrum (0.3–3 μm), the incident solar radiation dominates the thermally emitted radiation. The amount reflected depends on the physical and chemical composition of the earth's surface and atmosphere. This composition is what distinguishes types of earth surfaces and atmospheric constituents. Differences in composition generally make some components highly reflective (clouds, snow, and ice), others moderately reflective (deserts, barren land), and the remainder lowly reflective (ocean, vegetation) (Davis et al. 1984). This property can be used to detect the presence of some of these components by differences in their reflectance, that is, ''contrast signatures.''

Composition differences also cause these components to reflect solar radiation more efficiently in some parts of the spectrum than in others. This latter property can be used as a ''spectral signature'' to remotely detect the presence of certain surface–atmospheric components. For example, snow reflects very well at wavelengths below about 1 μm and very poorly beyond about 1.5 μm, while green vegetation reflects poorly below 0.7 μm but moderately well beyond 0.8 μm (Davis et al. 1984; Dozier and Warren 1982). Also, clouds tend to scatter sunlight uniformly with wavelength, whereas haze tends to scatter more at the shorter wavelengths (Nakajima and King 1990; Deirmendjian 1969).

Finally, the varying spatial structure of the earth–atmosphere composition can be used to differentiate between its different components, that is, ''spatial signa-

tures.'' For example, the ocean has a very uniform reflectance over hundreds of kilometers, whereas some clouds, mountainous terrain, and sparse vegetation have highly variable reflectances over tens of meters (e.g., Wielicki and Parker 1992).

In the thermal infrared, from about 3–20 μm, earth–atmosphere components may also be discriminated by these three types of signatures, but they result from a different physical process, absorption, and reemission of radiation, rather than from reflection and scattering. Infrared radiation is proportional to scene temperature, and thus contrast signatures are those that separate cold from hot surfaces, for example, clouds over deserts in the daytime. Spectral signatures are where the emissivity of surfaces vary with wavelength, such as between thin cirrus clouds and atmospheric water vapor in the 10–12-μm region of the spectrum (King et al. 1992). Finally, spatial signatures exist due to differences in scale between spatial inhomogeneities in the clouds and the underlying surface (Coakley and Bretherton 1982).

Cloud retrieval algorithms also generally separate themselves into daytime (solar reflectance and infrared emittance) and nighttime (infrared emittance only) algorithms. Because of the inherent differences in the two principal Earth surfaces, they also separate themselves by land and ocean. Each of these will be explored further in section 3, where a CLEAR/CLOUD classification algorithm is developed for global applications with NOAA AVHRR data, the CLAVR-1 algorithm.

3. Application of cloud detection signatures to global AVHRR data

Clear/cloud remote-sensing techniques employing the AVHRR are based on the following five spectral radiance-measuring channels. Channel 1 (centered at 0.63 μm) measures reflected visible radiation, which is weakly attenuated by ozone absorption and by molecular and particulate scattering. Channel 2 (centered at 0.83 μm) detects reflected near-infrared (NIR) radiation, which is moderately attenuated by water vapor, but less affected by molecular and particulate scattering. Channels 3, 4, and 5 (centered at 3.7, 10.8, and 11.9 μm, respectively) detect emitted radiation in the thermal IR, where attenuation is primarily by water vapor, increasing in strength as wavelength increases. Channel 3 is also sensitive to solar radiation reflected by the earth's surface and clouds, and it is only weakly attenuated by particulate scattering (Deirmendjian 1969).

The philosophy of applying these principles to AVHRR global data for operational real-time and retrospective derivation of climate-quality cloud products is based on the following requirements: 1) minimize auxiliary data to aid the classifications, thus reducing dependence of derived quantities on other independently measured climate variables, such as surface temperature; 2) avoid multiple passes through the data, which could provide AVHRR-specific information to aid in threshold setting, but increase processing time; and 3) base the algorithm on already proven operational real-time AVHRR cloud detection algorithms to increase the likelihood of success while minimizing development efforts.

This approach has led to the development of a multispectral, sequential, decision-tree threshold algorithm—CLAVR-1. The test thresholds do not vary with Earth location or season (universal), although some depend on infrared brightness (equivalent blackbody) temperature.

Past and current operational approaches at NOAA NESDIS use cloud detection algorithms that are application-specific, for example, the Multi-Channel Sea Surface Temperature (MCSST) (McClain et al. 1985), in that they discard information about the clouds themselves. CLAVR adopts a more ''generic'' approach, that is, one that works for all applications and one that detects clear and cloudy satellite observations over both land and sea, day and night, and even over snow, ice, and deserts.

Details of the CLAVR-1 daytime and nighttime cloud classification algorithms are described in the appendix, including comprehensive decision-tree flowcharts. In the present section the various cloud tests are grouped according to the type of ''signature'' test employed (see section 2). Discussion of the cloud test sequencing and thresholding, and tests for ambiguities, are also found in this section. Some threshold-setting details are discussed in the appendix.

a. Contrast signature tests

Thresholds are required in the application of contrast signature tests. The assignment depends on the earth surface type, cloud type, and whether the channel measures reflectance or emittance. The contrast signature tests all have the same characteristic: a pixel value is compared against a threshold value that is intended to separate cloudy pixels from all others. These thresholds can be determined either theoretically, empirically, or from past experience. Here it was chosen to set them empirically and from past experience, as it is very difficult to simulate all possible cloud–surface observation conditions with theoretical models.

1) REFLECTANCE TESTS

Some of the daytime tests use observed bidirectional reflectances. These reflectance factors (referred to as albedo) are derived from the observed signal for each pixel stored in the NOAA level 1b datasets using formulas and coefficients from Kidwell (1991). These reflectance factors are converted to equivalent-isotropic albedos by dividing by the cosine of the solar zenith angle and multiplying by the square of ratio of Earth–Sun distance at time of observation to the mean Earth–

Sun distance. They are further adjusted for calibration drift with time by the formulas of Rao and Chen (1995).

Two reflectance-based cloud tests have been developed for CLAVR-1. One utilizes the reflectance in channel 1 over land or in channel 2 over ocean and is referred to as the reflectance gross cloud test (RGCT). Another is the channel-3 albedo test (C3AT). A useful value for the channel-2 reflectance (R2) threshold for the RGCT over the ocean is 30%. Empirical studies have shown that this is a representative value for the albedo of homogeneous low-cloud fields and that it is not usually exceeded by specular reflection from the ocean. It also matches the cloud-filtering threshold used in processing for the NOAA AVHRR aerosol optical thickness product (McClain 1989). Over land the RGCT uses channel-1 reflectances (R1) instead of channel 2 because channel 2 is more sensitive to vegetation and is thus more highly reflective and variable, tending to minimize the contrast signature. A threshold of 44% has been found empirically to work well in detecting cloud over land. Gutman et al. (1995) confirm this RGCT threshold except for small areas in the Saharan desert in winter, where it can be exceeded. However, daytime temperature in desert areas is usually higher than expected for cloud, so such ambiguities can be removed. (See section 4c for description of restoral tests used to remove such ambiguities.)

The C3AT is introduced to detect weakly reflecting clouds (some cirrus or water clouds that are thin or subpixel in size). This test is also very useful in separating the effects of these weakly scattering clouds from atmospheric haze. This is because the larger cloud particles scatter sunlight more effectively than aerosol particles at 3.7 μm (Deirmendjian 1969). This test is used in a somewhat modified form in the operational aerosol retrieval program at NESDIS (McClain 1989). As the channel 3 radiance in daytime is a combination of emitted and reflected radiation, it is necessary to strip out the emitted portion using an estimate of it derived from channels 4 and 5. What remains is an estimate of the reflected radiance, which is converted into a channel 3 equivalent-isotropic albedo [see Eq. (A2) in the appendix]. Cloud-free land surfaces are appreciably brighter than the ocean. Accordingly, empirical C3AT thresholds have been found to be about twice the value used over the sea.

2) EMITTANCE TESTS

One emittance-based contrast signature test used in CLAVR-1 is the thermal gross cloud test (TGCT). Over the ocean the TGCT threshold is based on a limiting minimum infrared temperature for the ocean surface, namely, the freezing point of seawater. It will classify pixels as CLOUDY when the pixel's channel-4 temperature T_4 is below that of freezing seawater. Over land the TGCT threshold is lower than over the sea to prevent the potentially much colder land surfaces from being called CLOUDY. At latitudes where sea ice or snow is likely, contrast and spectral signature tests can be used to remove this ambiguity (see section 4c discussion of restoral tests). The value chosen for the TGCT threshold over land is 249 K. It is the minimum zonally averaged, cloud-free, land temperature observed equatorward of 60° latitude in daytime in the *Nimbus-7* cloud climatology (Stowe et al. 1989).

b. Spectral signature tests

Spectral signature tests involve the difference or ratio of the emittances or reflectances measured in two AVHRR channels. The two emittance channels (channels 4 and 5) and the combined emittance-reflectance channel (channel 3) have differing transparencies with respect to upwelling infrared radiation, principally because of water vapor in the atmosphere. The reflectance channels are more useful for resolving ambiguities (see section 4c).

1) REFLECTANCE TESTS

The ratio of channel-2–channel-1 reflectances (R2/R1) according to Saunders and Kriebel (1988) is less than 0.75 for a cloud-free ocean and is between 0.9 and 1.1 for cloud. The latter range is used for the reflectance ratio cloud test (RRCT) threshold. Over vegetated land surfaces, this ratio is typically greater than 1.2 (Gutman et al. 1995 show NDVI $>$ 0.1 for these surfaces, which is equivalent to R2/R1 $>$ 1.2), so the same threshold range for cloud detection works for these surface types as well. However, supporting empirical studies have shown that some desert surfaces have R2/R1 ratios in the cloud range, so the RRCT cannot be relied upon over such areas.

2) EMITTANCE TESTS

One emittance-type cloud/no-cloud threshold test is the channel 4–5 (four-minus-five Test—FMFT) brightness temperature difference. It is employed primarily to detect thin cirrus clouds (Inoue 1985; Prabhakara et al. 1988), which can produce larger FMFT values than possible from water vapor attenuation alone. This results from ice particles having a lower emissivity (higher transmissivity) at 10.8 than at 11.9 μm, creating an FMFT signature similar to that of water vapor. Depending on the thickness of the cirrus, this difference can exceed that due to water vapor alone. The FMFT can also be used to detect cold water droplet clouds in midlatitudes (Luo et al. 1995) and in polar latitudes (Yamanouchi and Kawaguci 1989), as will be explained in the discussion of restoral tests in section 4c.

The threshold for the FMFT must be chosen to unequivocally indicate the presence of cloud. This threshold is defined to be the maximum FMFT value that is attributable to water vapor alone. We have used the T_4

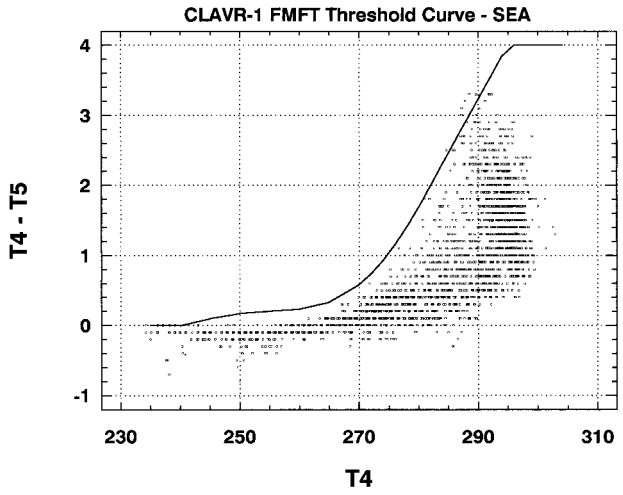

FIG. 1. Scattergram of channel-4 minus channel-5 (FMFT) brightness temperature difference vs channel-4 brightness temperature computed from raob's using a radiative transfer model to simulate AVHRR data (cloud-free ocean and cloud-free land combined). CLAVR-1 FMFT–sea threshold curve superimposed on data.

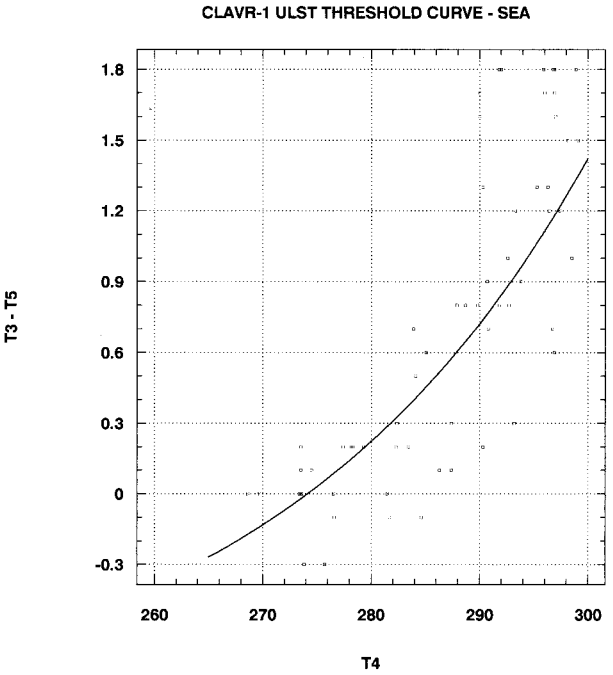

FIG. 2. Scattergram of channel-3 minus channel-5 (ULST) brightness temperature difference vs channel-4 brightness temperature ($T_4 > 271$ K) computed from raob's using a radiative transfer model to simulate AVHRR data for a cloud-free ocean at night. CLAVR-1 ULST–sea threshold curve superimposed on data.

$- T_5$ temperature-difference dependence on T_4 as an index of atmospheric humidity (cf. McClain et al. 1985; Saunders and Kriebel 1988). As we do not currently have a reliable method of extracting atmospheric water vapor from earth satellite data, we have generated a simulation database of calculated T_3, T_4, and T_5 brightness temperatures (accounting for each channel's spectral response function) from a large number of globally distributed cloud-free atmospheric soundings over ocean and land using radiative transfer theory. These results are plotted in a scatter diagram in Fig. 1, where the FMFT threshold for ocean is shown. It is essentially the same over land, but it extends to higher values beyond $T_4 > 295$ K. As T_4 increases, the maximum value of $T_4 - T_5$ also increases because warmer atmospheres can contain more water vapor. FMFT thresholds were defined by fitting fourth- or fifth-degree polynomials in T_4 to the maximum values of FMFT for these cloud-free conditions. The details can be found in section A4 of the appendix.

The radiative properties of cloudy and clear atmospheres at 3.7 μm differ from those at 10.8 or 11.9 μm; namely, clouds are more reflective and the atmosphere is more transparent at 3.7 μm (Hunt 1973), particularly in the case of low stratus clouds, which typically have very small droplet sizes. Based on prior success in cloud filtering for sea surface temperature estimates (McClain et al. 1985), a uniform low stratus test (ULST) based on channel-3 minus channel-5 temperature differences has proven a powerful nighttime test because the presence of cloud depresses $T_3 - T_5$ to substantially negative values (see Fig. A5 in the appendix). ULST requires a T_4-dependent threshold to allow for variable water vapor attenuation between the two channels. Using the same cloud-free simulation dataset, the ULST threshold curve, determined from a least squares fit through a subset taken from the ocean cases, is plotted in Fig. 2. The effect of water vapor absorption is again evident as an exponential increase in this temperature difference with increasing T_4. The figure is limited to $T_4 > 271$ K because it has been used extensively only over cloud-free and ice-free oceans. Its polynomial representation and other details can be found in section A4 in the appendix.

The relatively high optical transmittance of most cirrus clouds at 3.7 μm (Hunt 1973) combines with the increased dependence of the Planck blackbody radiance on temperature at this wavelength to yield large $T_3 - T_5$ differences for cirrus clouds. These temperature differences are the basis for a nighttime cirrus test (CIRT), which uses the function $(T_3 - T_5)/T_5$. Again, the cloud-free simulation database was used to define a T_4-dependent threshold for the CIRT to account for water vapor variations. These results are plotted in Fig. 3, again showing an increase in temperature difference with T_4. Analysis of the upper envelope of this relationship led to the threshold curve that is discussed in section A4 in the appendix.

c. Spatial signature tests

Spatial signature tests depend on the observation that, on the scale of 2×2 pixel arrays, the scene viewed by the AVHRR is relatively more ''uniform'' in the absence

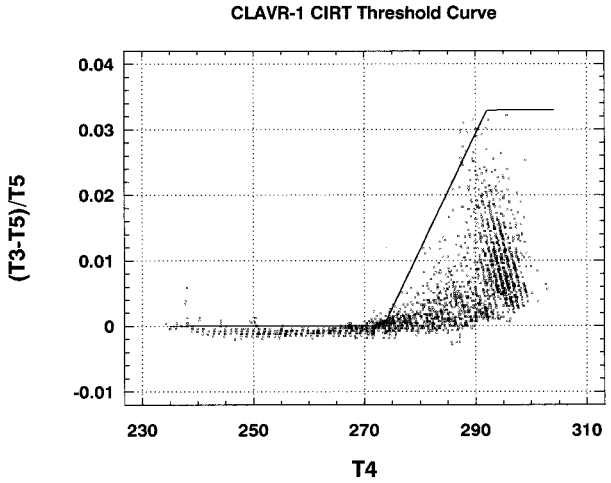

FIG. 3. Same as Figs. 1 and 2 except that $(T_3 - T_5)/T_5$ (CIRT) is plotted vs T_4. CLAVR-1 CIRT threshold curve superimposed on data.

of clouds than with clouds (McClain et al. 1985), and this is true whether reflectance (daytime) or emittance (daytime or nighttime) is used.

1) REFLECTANCE TESTS

Reflectance variability greater than 0.3% rarely occurs over cloud-free oceans in the absence of sun glint, so this is used for a reflectance uniformity test (RUT) threshold (McClain et al. 1985). Glint areas, however, are generally quite uniform thermally in the absence of clouds, so they are handled by a special ''restoral'' test (discussed in section 4c). Cloud-free land surfaces are naturally more variable in reflectance than ocean surfaces, therefore the RUT land thresholds must be greater than over the ocean. A value of 9% was derived empirically from image analysis studies. Mountainous regions may have spatial variability greater than this threshold and, without ancillary information, may be called cloud contaminated erroneously. As is the case with the RGCT (see section 3a), channel-2 reflectances are used for the RUT over ocean and channel-1 reflectances over land.

2) EMITTANCE TESTS

Experience has shown that when the ocean is cloud free it is almost always quite spatially uniform in the infrared. The thermal uniformity test (TUT) threshold, separating cloud free from cloud contaminated, has been found empirically to be 0.5 K over the oceans. This is slightly greater by 0.2 K than the threshold used in the operational MCSST algorithms (McClain et al. 1985). Over land, the maximum variability of channel-4 temperature (T_4) characteristic of cloud-free scenes has been found empirically to be six times larger than over the ocean because of the far less homogeneous thermal conditions and variable emissivities over land surfaces.

4. Cloud test sequencing for CLEAR/CLOUD classifications—The CLAVR-Phase I Algorithm

The various contrast, spectral, and spatial cloud signature tests described in the foregoing sections have been assembled into a sequential, decision-tree, multispectral threshold algorithm. This algorithm uses space/time-invariant (i.e., universal) thresholds either derived theoretically, empirically, or from past experience to identify CLEAR, MIXED, and CLOUDY 2×2 GAC pixel arrays. The algorithm sequence and thresholds have been optimized for four scene conditions: day/land, day/ocean, night/land, and night/ocean. The overall philosophy of the test sequences is to classify the clouds within each pixel array, first by their gross signatures and subsequently by their more subtle ones. This provides an algorithm that is efficient in computer time, and it ensures that pixels failing all the tests in the sequence have a very small probability of radiatively significant cloud cover in them. The precise choice of which cloud test should be first, second, etc., was first based on physical and meteorological reasoning. The sequencing was occasionally adjusted later based on experience with the algorithm and by analyzing test cases. Much prior experience with the MCSST algorithms was invaluable in this process. Ambiguities in classification are handled by what are called ''RESTORED-CLEAR'' tests. Specifics of the algorithm are described in the next three sections, with more detail provided in the appendix.

a. Daytime

The daytime (solar zenith angle $<84.3°$) ocean and land cloud test sequence, the display color used in section 5 to identify each test in an image, the AVHRR channels, and the test thresholds (with footnotes identifying how they were derived) are listed in Table 1. Also listed are the RESTORED-CLEAR tests and the colors used to describe the pixels classified as CLEAR. Also, two columns give the frequency of occurrence of this sequence of tests for one day [15 March 1985] (format: CLOUDY classification/MIXED classification). A flowchart description of the algorithm is found in the appendix, Figs. A1, A2 (ocean and land, respectively).

In general, a 2×2 pixel array is classified CLEAR only if all four pixels fail all the cloud tests listed. If any of the pixels pass any of these tests, the array is considered cloud contaminated. However, RESTORED-CLEAR tests (see section 4c) are applied to indicate ''possibly CLEAR'' (i.e., if the pixel could be cloud-free snow/ice, desert, or ocean viewed in the specular direction). If all four pixels in the array pass a cloud test and are not RESTORED-CLEAR, the array is called

TABLE 1. Daytime cloud test thresholds. Here, ''na'' means not applicable; ''t'' means trace, i.e., 0.0 < frequency (%) < 0.05; see Figs. A1–A2 for RESTORED-CLEAR test channels and thresholds. Footnotes—Thresholds determined: ''e'' = empirically; ''th'' = theoretically; and ''x'' = past experience.

	Land scene					Ocean scene			
				Frequency (%)				Frequency (%)	
	Color	Channel	Threshold	CLOUD	MIXED	Channel	Threshold	CLOUD	MIXED
CLOUD/MIXED tests									
RGCT	Red	1	>44%[e]	30.7	9.4	2	>30%[e]	30.6	13.7
RUT	Dk. blue	1	>9%[e]	na	7.4	2	>0.3%[x]	na	35.9
RRCT	Green	2/1	$0.9 < R < 1.1$[x,e]	1.7	1.6	2/1	$0.9 < R < 1.1$[x,e]	t	t
C3AT	Yellow	3, 4, 5	>6%[e]	1.4	1.7	3, 4, 5	>3%[x]	t	t
TUT	Lt. purple	4	>3 K[e]	na	13.3	4	>0.5 K[e]	na	2.2
FMFT	Pink	4, 5	>fcn T_4^{th}	16.4	3.7	4, 5	>fcn T_4^{th}	4.7	1.4
TGCT	Lt. blue	4	<249 K[e]	t	0.0	4	<271 K[x]	0.1	t
RESTORED-CLEAR tests									
C3AR		3	<3%[x]	na	na	3	<3%[x]	na	na
TUR		4	<1 K[e]	na	na	4	<0.5 K[e]	na	na
TGCR		4	>293 K[x]	na	na	na	na	na	na
CLEAR classes:									
CLEAR	Black			9.3				8.2	
RGCT restored	White			0.5				0.6	
RUT restored	Gray			0.5				2.6	
RRCT restored	Gold			0.9				t	
C3AT restored	Dk. purple			1.5				0.0	
	Total frequency (%)			100.0				100.0	

CLOUDY. If only one to three pixels follow this path, the pixel array is called MIXED. This classification implies a mixture of cloudy and cloud-free pixels, or fully cloudy pixels with variable cloud heights/thicknesses, or partly cloudy pixels with varying cloud properties within the 2×2 array. For the same reasons, a pixel array that passes a spatial signature test (uniformity) is also classified MIXED. As is evident in the distribution of cloud test occurrences in Table 1, the most powerful cloud tests are the contrast and spatial signature tests, with the spectral signature tests assisting with detection of cloud types weakly affecting the radiation field (e.g., thin cirrus).

A better sense of the algorithm can be obtained from the flowcharts (Figs. A1, A2) presented in the appendix. Except for threshold values, the ocean and land daytime algorithms are essentially the same. The RGCT detects thick clouds and the RUT detects thinner, horizontally nonuniform cloud. The RRCT and the channel-3 albedo test (C3AT) detect thinner, horizontally uniform clouds, identifying clouds missed by the previous tests. The latter is particularly good at separating cloud from haze. The RRCT and C3AT are bypassed over deserts because they cannot unambiguously detect clouds over these surfaces. Also, the C3AT is skipped when within the cone of specular reflection (see section 4c). Three thermal tests follow these reflectance tests to detect clouds too optically thin to be classified as cloud by them. In sequential order, TUT detects nonuniform cloud, FMFT detects optically thin cirrus, and finally, TGCT detects thicker cloud (the latter test is excluded near the poles). The cloud tests that use channels -3, -4, or -5 temperatures are suspended when the channel-4 temperature exceeds 315 K because these channels saturate and cannot be used reliably in such conditions. The day and night RESTORED-CLEAR logic is described in section 4c.

b. Nighttime

Cloud test sequencing at night is again the same for ocean and land, only the thresholds and treatment of desert surfaces are different. It is also much simpler than the daytime sequencing. There are only emittance tests. The test sequence for land and ocean is given in Table 2, which contains information similar to that Table 1. At night, the sequence begins with TGCT, which detects thick cold clouds. This is followed by TUT, which serves the same function as it did in daytime, to detect nonuniform cloud not cold enough to be detected by the prior TGCT. As in the daytime, the contrast and spatial signature tests account for between about 60% (land) and 80% (ocean) of the classifications. The next test in the sequence is ULST, which is able to detect low-altitude, water-droplet clouds, primarily over oceans, as is seen by the frequencies in Table 2. Because of reduced emissivity of deserts at 3.7 μm and also because of poor channel-3 precision at very low temperatures, this test is suspended over deserts or when temperatures fall outside the range 271–289 K over land [see Eq. (A4) in the appendix]. FMFT serves the same purpose as it does in daytime, detection of thin cirrus. As in the daytime, it is much more effective at doing this over land, partly because the land sequence allows more pixels to be

TABLE 2. Nighttime cloud test thresholds. Here, ''na'' means not applicable; ''t'' means trace, i.e., 0.0 < frequency (%) < 0.05; see Figs. A3–A4 for RESTORED-CLEAR test channels and thresholds. Footnotes—Thresholds determined: ''e'' = empirically; ''th'' = theoretically; and ''x'' = past experience.

	Land scene					Ocean scene			
				Frequency (%)				Frequency (%)	
	Color	Channel	Threshold	CLOUD	MIXED	Channel	Threshold	CLOUD	MIXED
CLOUD/MIXED tests									
TGCT	Red	4	<249 K[e]	42.2	6.3	4	<271 K[x]	44.5	6.2
TUT	Dk. blue	4	>3 K[e]	na	15.6	4	>0.5 K[e]	na	33.1
ULST	Yellow	3, 5	<fcn T_4^{th}	0.5	0.3	3, 5	<fcn T_4^{th}	5.7	1.5
FMFT	Pink	4, 5	>fct T_4^{th}	10.7	4.1	4, 5	>fcn T_4^{th}	0.1	0.1
CIRT	Lt. purple	3, 5	>fct T_4^{th}	2.2	3.1	3, 5	>fcn T_4^{th}	0.2	0.2
RESTORED-CLEAR tests									
FMFR		4, 5	<fcn T_4^{th}	na	na	4, 5	<fcn T_4^{th}	na	na
CLEAR classes									
CLEAR	Black			13.0				8.2	
FMFR restoral	Black			2.0				0.2	
Total frequency (%)				100.0				100.0	

tested. The final test is the CIRT, which uses the Channels 3–5 brightness temperature differences to detect thin cirrus. This test is bypassed if the channel-1 digital count value is greater than 45 (its dark scene value is typically about 40 counts) because this indicates the presence of stray light contaminating the AVHRR data. This is prone to occur late in the lifetime of each satellite, and the stray energy erroneously elevates the channel-3 temperatures, giving false thin cirrus cloud classifications.

The nighttime decision trees are also simpler than the daytime ones in that they have only one restoral test (described in section 4c). As in the daytime algorithms, the classification of 2 × 2 arrays as CLEAR, MIXED, or CLOUDY depends on testing the four pixels in each array. More detail is given in the appendix, where flowcharts to help illustrate the process of the nighttime algorithms are presented in Figs. A3, A4 (ocean and land, respectively).

c. Treatment of ambiguous classifications (RESTORED-CLEAR)

There are situations in which a given cloud test can be passed erroneously, for example, when snow, ice, or sun glint yields a channel-1 or -2 reflectance that exceeds the RGCT threshold. When this happens, it is sometimes possible to ''restore'' the pixel array to a path on the decision tree (see flowcharts in Figs. A1–A4 in the appendix) that could eventually lead to a CLEAR snow/ice, land, or ocean classification (provided no subsequent ''restored cloud'' tests are passed). For this to happen, all four pixels of the 2 × 2 array must pass the restoral test. Although the typical frequency of occurrence of RESTORED-CLEAR classifications, as indicated in Table 1, is quite small, they can be important in obtaining an accurate portrayal of cloud-free conditions. The next two sections briefly describe the various restoral tests used in CLAVR-1 and details for daytime are covered in section A6 in the appendix.

1) DAYTIME RESTORAL TESTS

When a 2 × 2 array is highly reflective in channel 1 or 2 and relatively dark in channel 3, it is considered likely to be a CLEAR array situated over snow or ice. Consequently, applying a channel 3 albedo test provides a mechanism for restoring these potentially CLEAR pixels to a RESTORED-CLEAR classification after they have erroneously passed either RGCT, the RUT, or the RRCT cloud tests (see Figs. A1, A2 in the appendix).

Deserts and other arid land types can have surface albedo conditions that satisfy any of the four reflectance-based cloud tests. If these land types are actually cloud free, however, they usually have brightness temperatures that exceed those associated with clouds, at least for the afternoon satellites (*NOAA-7, -9, -11, and -14*). Thus, to remove this ambiguity, all pixels passing these tests are subjected to a thermal gross cloud restoral (TGCR) test. Any MIXED or CLOUDY array where all four pixels have T_4 greater than the TGCR threshold are classified as RESTORED-CLEAR. Because some nondesert land surfaces exhibit channel 3 albedos greater than the C3AT threshold, pixels passing the C3AT are also subjected to a thermal uniformity restoral (TUR) test before the TGCR is invoked. If the 2 × 2 pixel array is sufficiently uniform thermally, it is classified RESTORED-CLEAR and a specific cloud code is assigned to indicate this path.

In an attempt to remove the sun glint–related ambiguity that can be present in all four reflectance tests over the ocean, a TUR test (in this case using a limit of < 0.5 K) is applied when the satellite is viewing within

the expected region of specular reflection (see section A5 in the appendix).

To increase the probability that RESTORED-CLEAR pixel arrays are CLEAR, they are subjected to several infrared cloud tests. First TUT is applied (with the threshold set to 3 K) over ocean as well as land, as sea ice is likely to be as nonuniform as land. They are also subjected to an FMFT and, over nonpolar land, a TGCT. The former looks for thin cirrus and the latter for deep glaciated clouds, both of which may exhibit low channel 3 albedos because of their ice content. If any of these tests is passed, the pixel array is considered MIXED or CLOUDY (if all four pixels pass the test) and the cloud codes are modified to indicate the decision-tree path followed (see flowcharts, Figs. A1, A2, in the appendix).

2) NIGHTTIME RESTORAL TESTS

The nighttime algorithm has provision for only one type of RESTORED-CLEAR classification, namely, one allowing for erroneous passing of the TGCT. The use of a constant threshold for the TGCT has the potential for misclassification of pixels at high latitudes where cloud-free, usually snow- or ice-covered, surfaces can reach temperatures low enough to be classified CLOUDY. As shown by Yamanouchi and Kawaguci (1989), low water clouds over ice- and snow-covered surfaces can be detected by positive channel 4–5 temperature differences (viz., check if brightness temperature difference between channels 4 and 5 is greater than a channel 4 temperature-dependent FMFT threshold). Therefore, all TGCT CLOUDY pixels poleward of 30° latitude, ocean or land, are subjected to a four-minus-five restoral (FMFR) test. If this test is passed by all four pixels, the pixel array is RESTORED-CLEAR and passes on to TUT and subsequent cloud tests in the sequence.

5. Initial evaluations of the algorithm

This section shows examples of the performance of the CLAVR-1 algorithm, first, on a qualitative, test-by-test basis, second, on a quantitative basis where CLAVR-1 values of cloud amount are correlated with an independent estimate in fixed geographical areas by an interactive image processor. An evaluation on a global basis by statistical comparisons with other published satellite cloud climatologies has been published (Hou et al. 1993) and will also be the subject of future publications.

a. Qualitative evaluations of cloud tests

Cloud tests from the CLAVR-1 decision-tree sequences were evaluated using 5 daytime and 11 nighttime GAC scenes. Some were over land and others over the ocean; and some were in winter and others in summer. Geographically they varied from Somalia and Saudi Arabia to the western United States and adjacent waters, and from eastern Siberia to Antarctica. Lack of space permits detailed discussion of only a few of these scenes, but the analyses of all are summarized later in this section. They all show that the CLAVR-1 tests are performing their function of separating clear from cloudy pixels over most times and locations on the earth.

1) SOMALIA AREA

Photointerpretation of Fig. 4a, a standard black-and-white image of channel-2 reflectance over the coastline of eastern tropical Africa on 9 July 1986 indicates that over the ocean there are mainly scattered, small-scale clouds characteristic of weak convection. There is some tendency toward mesoscale organization, yielding somewhat stronger convective patterns with elements that are more reflective. The associated channel-4 thermal IR image (not shown) indicates, however, that the brighter and more organized cloud masses are little, if any, deeper (i.e., colder) than the more scattered ones. Figure 4b, the same image rendered in color to depict the CLAVR-1 cloud classifications (see Table 1, which shows the color used to depict each cloud test), reveals that the better-organized cloudy areas over the ocean are detected by the first daytime reflectance test (RGCT), the remainder are classified either as CLEAR (black) or MIXED due to nonuniformity of reflectance (RUT). Figure 4c depicts the distribution of MIXED and CLOUDY pixel arrays, which are subsequently used in the estimation of cloud cover (cf. sections 4b and 4c), where a gray shade has been assigned to the MIXED class and a white shade to the CLOUDY class.

Figures 4b and 4c indicate which test detected the presence of cloud and whether that array was considered MIXED or CLOUDY. In a careful study of the clouds in scene A of Fig. 4a, the preponderance of 2×2 pixel arrays were classed as MIXED, with only 8% called CLOUDY and 9% CLEAR. All the CLOUDY ones passed the first test, the RGCT, so the other CLAVR-1 tests were never applied.

Photointerpretation of land scene B in Fig. 4a shows more widespread cloudiness than was the case over the sea, although again there appears to be no well-organized synoptic-scale or deep convective cloud systems present. The MIXED cloud amount category predominates as seen in Fig. 4c, although perhaps not as much as over the ocean. Some differences in cloud type do show up between land and sea in Fig. 4b, however. Because the threshold for the first reflectance test is higher over land, some CLOUDY/MIXED pixels passed other tests (RRCT, C3AT, and TUT). Likewise, some pixels classed as CLEAR resulted from the thermal restoral process (TGCR). In scene B, the majority of the pixel arrays (68%) were classified as MIXED, although almost 14% were called CLOUDY and about 17% were CLEAR or RESTORED-CLEAR (about 1%). CLAVR-1 classified the CLOUDY arrays mostly on the basis of

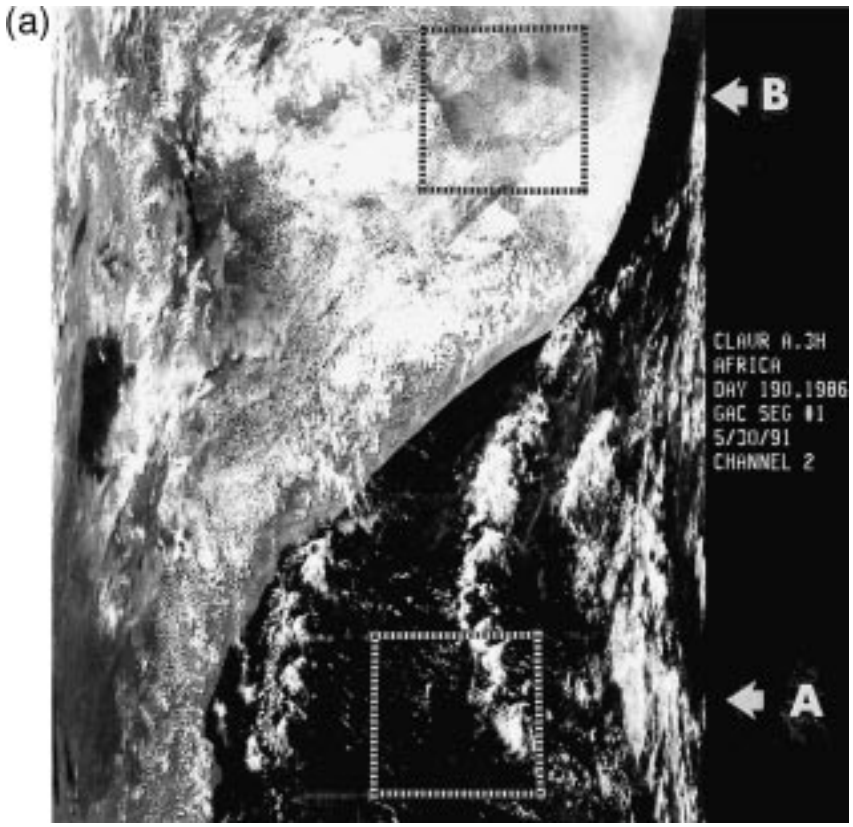

FIG. 4a. Grayscale cloud image of an orbital segment of AVHRR channel 2 GAC reflectance data over eastern tropical Africa in daytime. The location of two test scenes is shown.

the RGCT, but a significant number were from the RRCT.

2) SOUTHWESTERN UNITED STATES

Three nighttime scenes in the southwestern United States (F, G, and H) are depicted in Fig. 5a. They are part of a channel-4 (10.8 μm) brightness temperature GAC image (low temperatures are white) from a descending segment of an orbit on 9 July 1986. Scene F is entirely over land in the high plateau area, whereas G is mostly over the ocean just off the California coast. Scene H is farther north along the coast, but virtually completely over land. Figures 5b and 5c are of the same type as Figs. 4b and 4c.

Photointerpretation of the ocean portion of Fig. 5a is made difficult by a lack of thermal contrast between any low-level clouds present and the underlying ocean surface. The coldest clouds are well inland and appear as several organized clusters or bands, some portions of which are convective in appearance. There is a fairly substantial amount of cloud-free land area, which is classified as CLEAR by the CLAVR-1 algorithm (see Figs. 5b and 5c). The scattered distribution of MIXED arrays in this image, most noticeable in Fig. 5c, is probably the result of terrain-induced effects vis a vis the channel-4 TUT. The deeper and more organized convective clusters over land, as well as a more stratified-appearing cloudy area near the coast (middle and upper-left edge of Fig. 5b), are easily detected from their low temperatures (TGCT). Most noteworthy, however, is that low-level stratus over the ocean has been detected by the ULST spectral-signature test (lower-left edge of Fig. 5b). The presence of this type of cloud in this area is consistent with surface-based climatology (Warren et al. 1988). Other low stratus (yellow) patches are seen over land in Fig. 5b, the largest is located in the upper-right corner in area F. One other CLAVR-1 cloud type, thin cirrus (FMFT), is found in this segment in significant amounts but over rather limited areas.

A statistical analysis shows that CLAVR-1 classified scene F as predominantly MIXED (55%) or CLEAR (34%), with the CLOUDY (11%) areas being predominantly made up of low stratus (58%) or thin cirrus (25%). The MIXED pixel arrays result predominantly from TUT (76%). The thin cirrus arrays (FMFT) are mostly associated with a layer of clouds colder than the low stratus arrays. The low stratus classification may also partially be the result of surface emissivity differences between the 3.7- and 10.8-μm parts of the spectrum. There were only a few very cold (TGCT) CLOUDY arrays (with T_4 around 240 K), which would

(b)

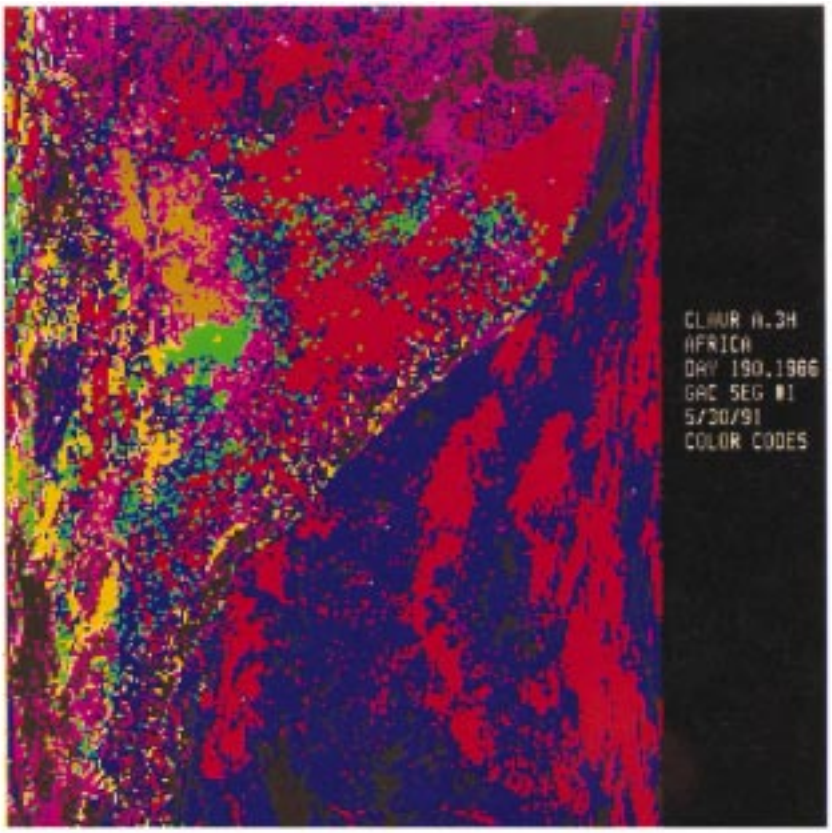

(c)

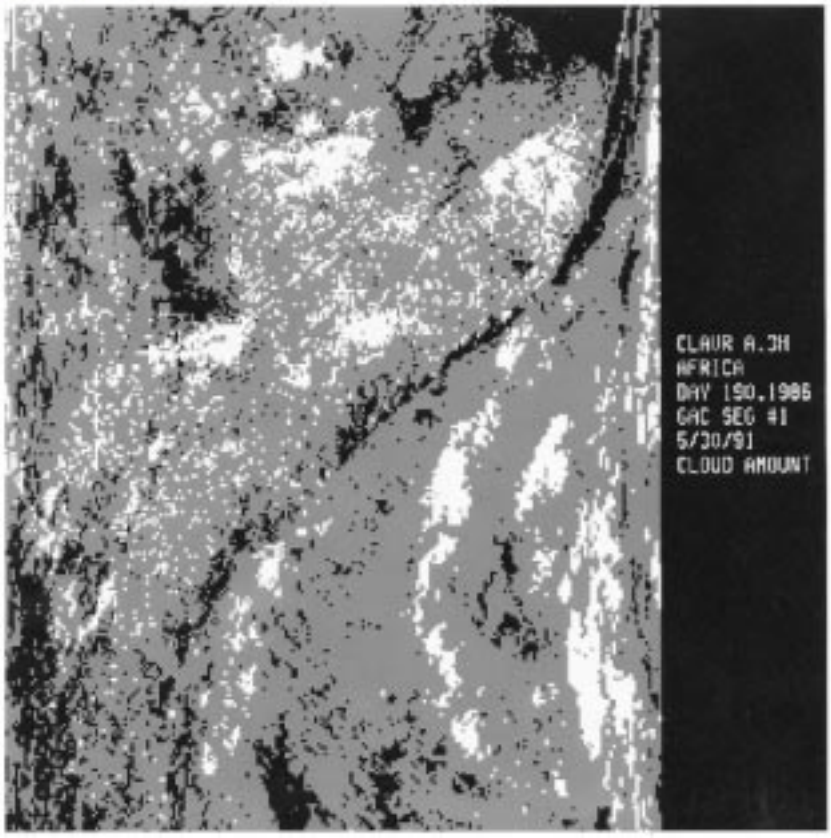

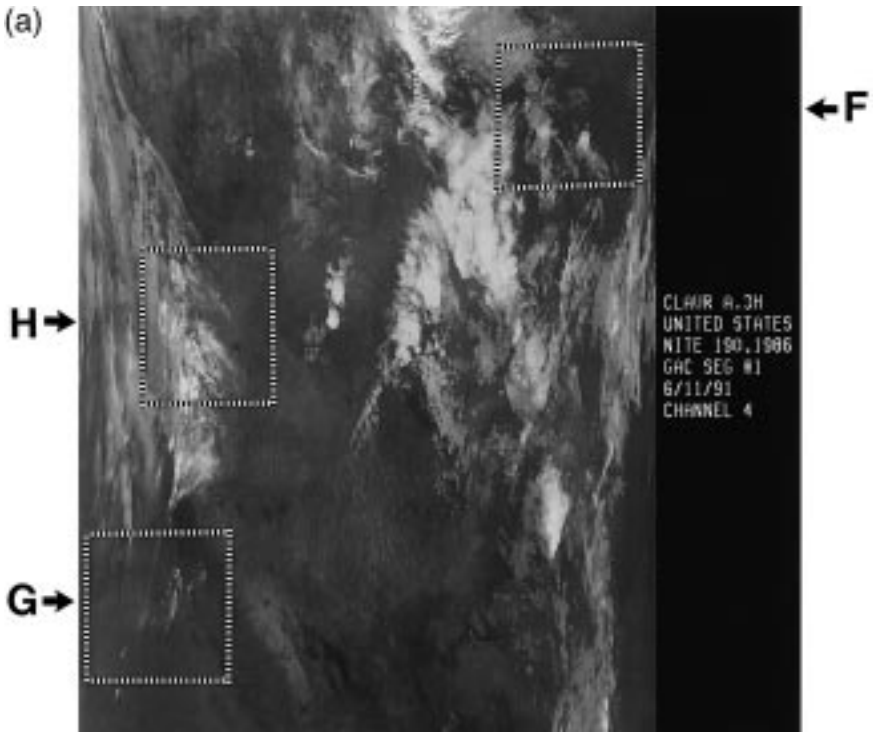

FIG. 5a. Grayscale cloud image of an orbital segment of AVHRR channel-4 GAC temperature data over the southwestern United States in the nighttime. The location of three test scenes is shown.

indicate rather thick high clouds. There were thin cirrus clouds identified by the CIRT, but these were not very spatially extensive (mostly MIXED category), and were rather warm ($T_4 \sim 281$ K). Figure 5a shows that these thin cirrus clouds are associated with temperatures lower than the surrounding surface area, which according to Luo et al. 1995, had a brightness temperature of 284.3 K.

The nighttime, mostly ocean scene G is seen in Fig. 5c to be classified by CLAVR-1 about equally into each of the three coverage categories. Figure 5b shows that of the CLOUDY cases, low stratus clouds (ULST) predominate overwhelmingly (99%), with the remaining 1% being colder (TGCT). The CLEAR pixels over the ocean were chiefly in a narrow range of channel-4 temperature around 282 K, whereas over the coastal land area, the associated T_4 varied from 275 to 291 K. The low stratus appeared to be in several layers or thickness regimes, ranging in T_4 from 278.5 to near 283.5 K, which was actually warmer than the immediate clear ocean.

Qualitative evaluations of scenes in this area indicate that low stratus clouds are diagnosed effectively at night by the ULST, especially over the sea, even where the stratus-top temperatures are within a few degrees (higher or lower) of the sea surface temperature. Over land, colder clouds were detected by FMFT. Our interpretation of these as always being thin cirrus is questionable, however. We have conducted studies that show that clouds cold enough to be detected by the TGCT would also have been detected by the FMFT, implying that these clouds, if cirrus, are not very thin. It is as likely that they are midlevel water clouds, as pointed out by Luo et al. (1995). This evaluation indicates that, although rare in occurrence, when thin cirrus is indicated by CIRT, it indeed appears to be thin. This is evidenced by the associated channel 4 temperatures being much closer to the cloud-free earth-surface temperature than is the case with clouds detected by FMFT. Many of the CIRT classifications were of the MIXED category, implying that the higher temperatures may also be indicative of cloud not filling the radiometers field of view.

3) SCENES IN OTHER AREAS

Several nighttime scenes in the northeast Africa/Saudi Arabia (not shown, but including a portion of the Red

←

FIG. 4. (b) Color-coded image of the same segment derived from the CLAVR-1 algorithm. Refer to Table 1 and Figs. A1 and A2 to relate color to clear/cloud classification and algorithm path. (c) CLAVR-1 classification of the same segment into three categories of cloud cover: CLOUDY (white), MIXED (gray), and CLEAR (black).

(b)

(c)

Sea) region from 9 February 1990 were studied because their channel-4 images suggest the presence of large bands or areas of cirrus with little or no other type of cloud present. It was determined that when cold enough to be classified as CLOUDY by the TGCT, either of the two thin cirrus tests (FMFT or CIRT) would also have detected this variably thick cirrus. All clouds not detected by the TGCT were detected by either the FMT or CIRT, supporting the foregoing image interpretation.

Several scenes in eastern Siberia in February 1990 were examined in some detail with respect to the performance of the FMFT, ULST, and CIRT in polar areas at night. One important finding is that the threshold used in the restoral test (FMFR) to detect cloud-free surfaces colder than the TGCT threshold is not optimum. It would perform better if the threshold was a few tenths of a degree higher. A similar adjustment to the CIRT threshold, which calls some apparently cloud-free areas CLOUDY, appears needed. Finally, it was found that the lower cutoff temperature for application of the ULST over land is probably set too high, as this test appears to have detected low stratus clouds over land at channel-3 temperatures as low as 240 K.

A number of daytime LAC (local area coverage: pixel size 1.1 km $\times$ 1.1 km at nadir) scenes have also been studied. To illustrate the CLAVR-1 algorithm's ability to discriminate between snow/ice and cloud, one case from the Antarctic coast on 23 December 1986 is shown in Fig. 6a (channel 2 reflectance). With the predominance of sea ice and shelf ice in this image, and with the reflectance of this ice being comparable to that of clouds, it is difficult to distinguish the latter from the ice surfaces. Only some very dark areas, mostly just off the Antarctic ice shelf in the upper (southern) part of the image, are easily interpreted because they appear to be free of both ice and clouds. There are what appear to be clouds in the lower portion of the image. A considerably more definitive separation of ice from liquid water clouds is afforded by using the channel-3 albedo restoral (C3AR) in the CLAVR-1 algorithm (see Fig. 6b, a colorized image of the cloud classifications). Recall that ice or snow is not as reflective as water clouds in channel-3, so RESTORED-CLEAR by the C3AR (white) serves well in distinguishing CLOUDY pixels (RGCT and FMFT) over snow or ice. However, thick ice-particle clouds in polar regions cannot be separated unambiguously from CLEAR ice or snow with the CLAVR-1 algorithm because the spectral signatures of the two surfaces are too similar.

b. Quantitative evaluation of cloud amount

To assess the accuracy of cloud amount estimates made from CLAVR-1 classifications, a surface/cloud ''truth'' pixel analysis is provided using an image processor to display contrast-enhanced scenes derived from LAC or GAC data. Analysts interact with the imaged data by using the processor to independently estimate the amount of cloud in a fixed geographical area.

Historically, the detection and quantification of cloud cover from environmental satellite imagery has employed statistical analysis of the digital data rather than direct examination of the imagery (Coakley and Bretherton 1982; Rossow and Garder 1993). As part of the development of the CLAVR-1 algorithm, in which the main thrust is an accurate delineation of CLEAR 2 $\times$ 2 GAC pixel arrays, a cloud ''masking'' capability was developed using contrast-signature threshold tests programmed into an image processor. The masks are exactly registered and superimposed upon a 100 $\times$ 100 pixel segment of an image from AVHRR channels 1, 2, or 4. This system thus provides a means for visually masking the clouds interactively and computing that fraction of the segment interpreted to be covered by clouds by the analyst. Given a cloud amount output from the CLAVR-1 algorithm for this same segment enables a quantitative comparison of the two independent estimates of cloud cover amount. Although the analyst's cloud amounts cannot be expected to be perfect truth, a previous study indicated that an analyst can estimate fractional cloud amount with an accuracy of 0.05–0.10 in daytime and 0.10–0.15 at night (Stowe 1984).

The foregoing procedure for comparing computer and human estimates of cloud amount has been euphemistically dubbed ''cloudbuster.'' The initial CLAVR-1 algorithm, when used to estimate cloud amount, assigns 50% cloud cover to all 2 $\times$ 2 pixel arrays classified as MIXED, and 0% and 100% for the CLEAR and CLOUDY arrays, respectively. This algorithm is termed the fifty-fifty split (FFS) algorithm. The statistics reported here use intercomparison datasets from five GAC data scenes; three are daytime and two are nighttime. Although 20–25 (100 $\times$ 100 pixel) segments were defined for most scenes, one had only 12. The segments covered land, ocean, and coastal regions.

For all daytime segments, the following linear regression statistics (Stowe 1984) were computed (see Table 3): mean cloud amounts from cloudbuster and from the CLAVR-1 algorithm, along with their associated standard deviations; the root-mean-square error; the random error (regression standard error/$2^{1/2}$); and the bias

←

FIG. 5. (b) Same segment shown in (a) but showing color-coded classifications derived from the CLAVR-1 algorithm. Refer to Table 2 and Figs. A3 and A4 to relate color to CLEAR/CLOUD classification and algorithm path. (c) CLAVR-1 classification of the same segment into three categories of cloud cover: CLOUDY (white), MIXED (gray), and CLEAR (black).

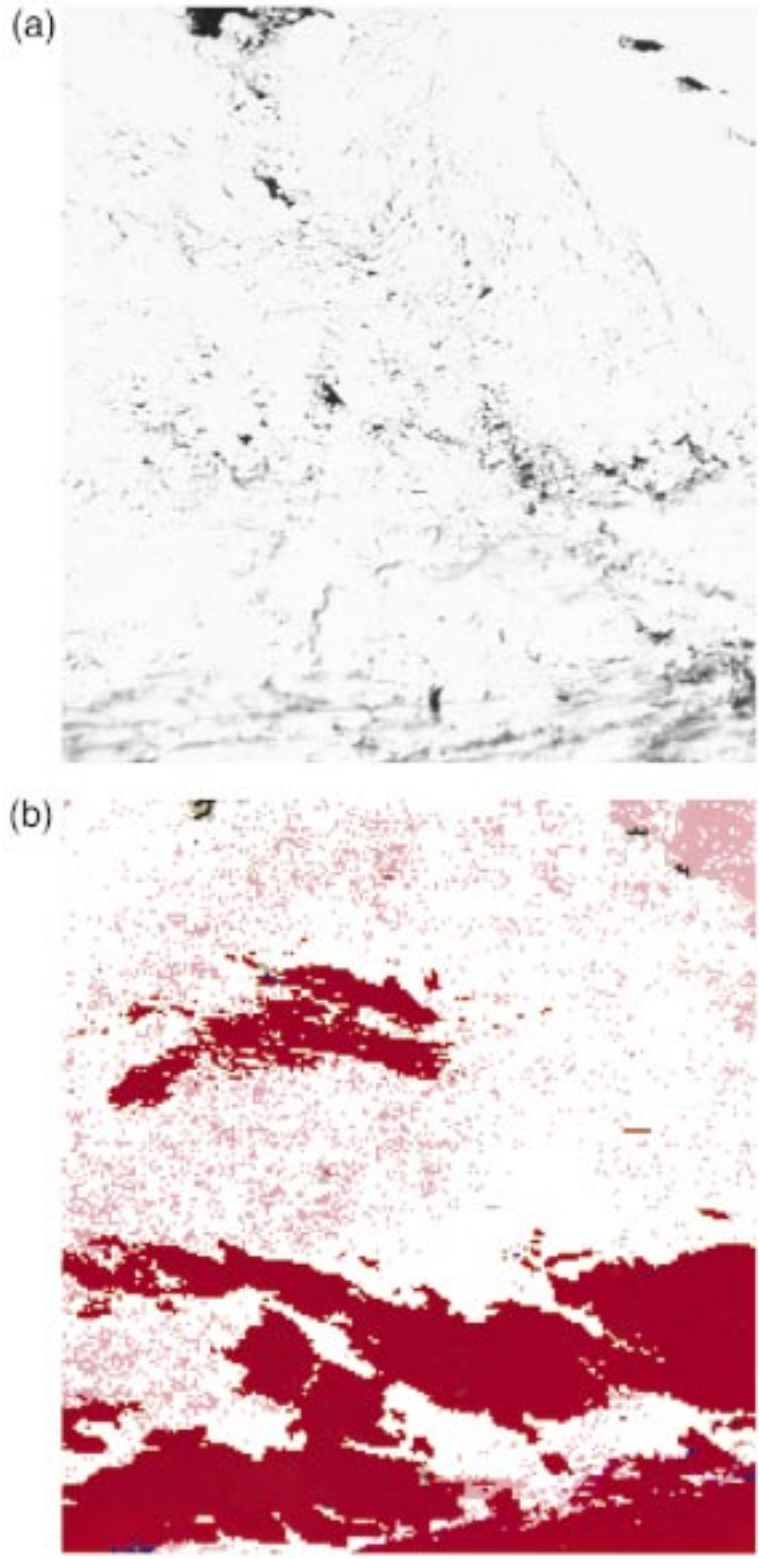

FIG. 6a. Grayscale cloud image of an orbital segment of AVHRR channel 2 LAC reflectance data over an Antarctic coastline. Fig. 6b. Same segment shown in Fig. 6a but showing color-coded classifications derived from the CLAVR-1 algorithm. Refer to Table 1 and Figs. A1 and A2 to relate color to CLEAR/CLOUD classification and algorithm path.

TABLE 3. Statistics from cloudbuster intercomparisons.

	Daytime		Nighttime	
	Cloudbuster	CLAVR	Cloudbuster	CLAVR
Mean	47.1	49.1	39.2	43.3
Std. dev.	23.9	14.4	27.6	22.6
Sample size	51.0		40.0	
rms error	15.5		10.5	
Random error	10.7		6.5	
Correlation coef (%)	79.0		95.0	
Bias (0)	11.8		9.4	
Bias (mean)	2.0		4.1	
Bias (100)	−9.1		−4.1	

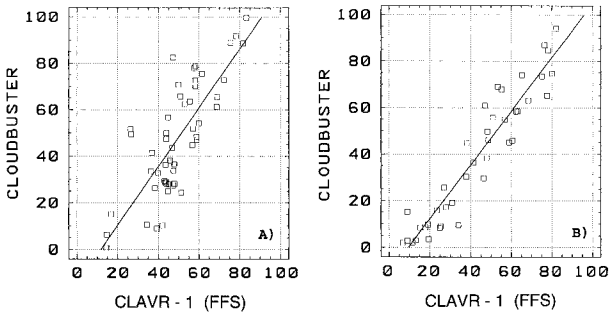

FIG. 7. Regression relationship between cloudbuster (interactive computer estimate) and CLAVR-1 cloud amount (FFS method) for 100 × 100 GAC pixel arrays from sample daytime and nighttime test images. These arrays were chosen from land, ocean, and coastal regions.

(difference of the means) of CLAVR-1 relative to cloudbuster. An overestimate by the CLAVR-1 algorithm would give a positive bias and an underestimate a negative one. Also calculated using the regression line slope and intercept was the projected bias if the cloudbuster cloud amount was 0% [bias(0)] and if it was 100% [bias(100)].

The bias(0) and bias(100) statistics in Table 3 demonstrate that the CLAVR-1 FFS cloud amount algorithm tends to overestimate the cloud amounts when cloudbuster classifies them as small and to underestimate when cloudbuster classifies them as large. Figure 7 shows the CLAVR-1 mean values plotted against the cloudbuster cloud amounts for the two groupings of data discussed above. It illustrates the general tendency for the CLAVR-1 FFS algorithm to overestimate the fractional cloud cover about 0.10 when it is small and to underestimate it by between 0.05 and 0.10 when it is large. This bias was also detected globally in a study comparing different cloud algorithms (Hou et al. 1993).

This is an expected consequence of MIXED (partly cloudy) pixel arrays, which tend to be less than 50% cloud covered when cloud amounts are small and greater than 50% when cloud amounts are large, as reported by Molnar and Coakley (1985). They use this property of MIXED pixels to derive a formula that effectively reduces this cloud amount bias in a statistical mean sense from regional (grid cell) estimates of cloud amount. We call this method the statistically equivalent spatial coherence (SESC) algorithm. It computes fractional amount of cloud within each grid cell as

$$A_T = N_0/N_T + [0.5 + 0.5(N_0/N_T - N_C/N_T)]N_M/N_T,$$

where A_T is total cloud amount; and N_C, N_M, and N_0 are the populations of pixels with CLEAR, MIXED, and CLOUDY classifications. The variable N_T is the total pixel count. As is evident from the equation, the SESC algorithm decreases cloud cover relative to the FFS method when the proportion of CLEAR pixels exceeds the proportion of CLOUDY pixels (term in parenthesis is negative) and increases it when the proportion of CLOUDY pixels exceeds the CLEAR pixels. To quantify this improvement over FFS, linear regression coefficients relating the FFS estimate to SESC for both ascending (daytime) and descending (nighttime) daily global data have been computed for one day. These have been substituted into the regression equation relating cloudbuster to FFS to estimate the slope and intercept relating cloudbuster to SESC. This exercise yields a bias(0) of +2.6% and a bias(100) of +0.6% for daytime, and a bias(0) of +0.1% and a bias(100) of +4.2% for nighttime for the SESC result relative to cloudbuster. Thus, the SESC cloud amounts are less biased than the FFS values (see Table 3).

An independent assessment of the cloud amount biases in the FFS and SESC methods has been performed by Luo et al. (1999, manuscript submitted to *J. Atmos. Oceanic Technol.*) who compares these two cloud amount estimates with a more sophisticated interactive computerized image analysis for 36 1° latitude/longitude cells in the FIRE-II study area covering parts of Kansas and Oklahoma on the afternoon of 28 November 1991. Using the same statistical methods as in Table 3, these regression results give an FFS bias(0) of 26.1% and a bias(100) of −25%, whereas the SESC bias(0) is 20.8% and the bias(100) is −12%. Although these results are only for one day in relatively small geographical areas and tend to be larger than when compared with cloudbuster, they still show that the SESC method gives cloud amounts in better agreement with interactive image analysis techniques than FFS.

In summary, putting more emphasis on the cloudbuster analysis of FFS coupled with the global relationship between FFS and SESC cloud amounts because of the greater range of conditions over which those statistics have been acquired, we conclude that on average the CLAVR-1 SESC fractional cloud amount should be within about 0.05–0.10 of the values estimated by interactive image analysis.

To illustrate the characteristics of global cloud cover as derived by the CLAVR-1 SESC method, the monthly mean (ascending plus descending) cloud amount for September 1989 is shown in Fig. 8. This date was chosen to be consistent with analyses presented in a companion CLAVR paper (Vemury et al. 1999, manuscript

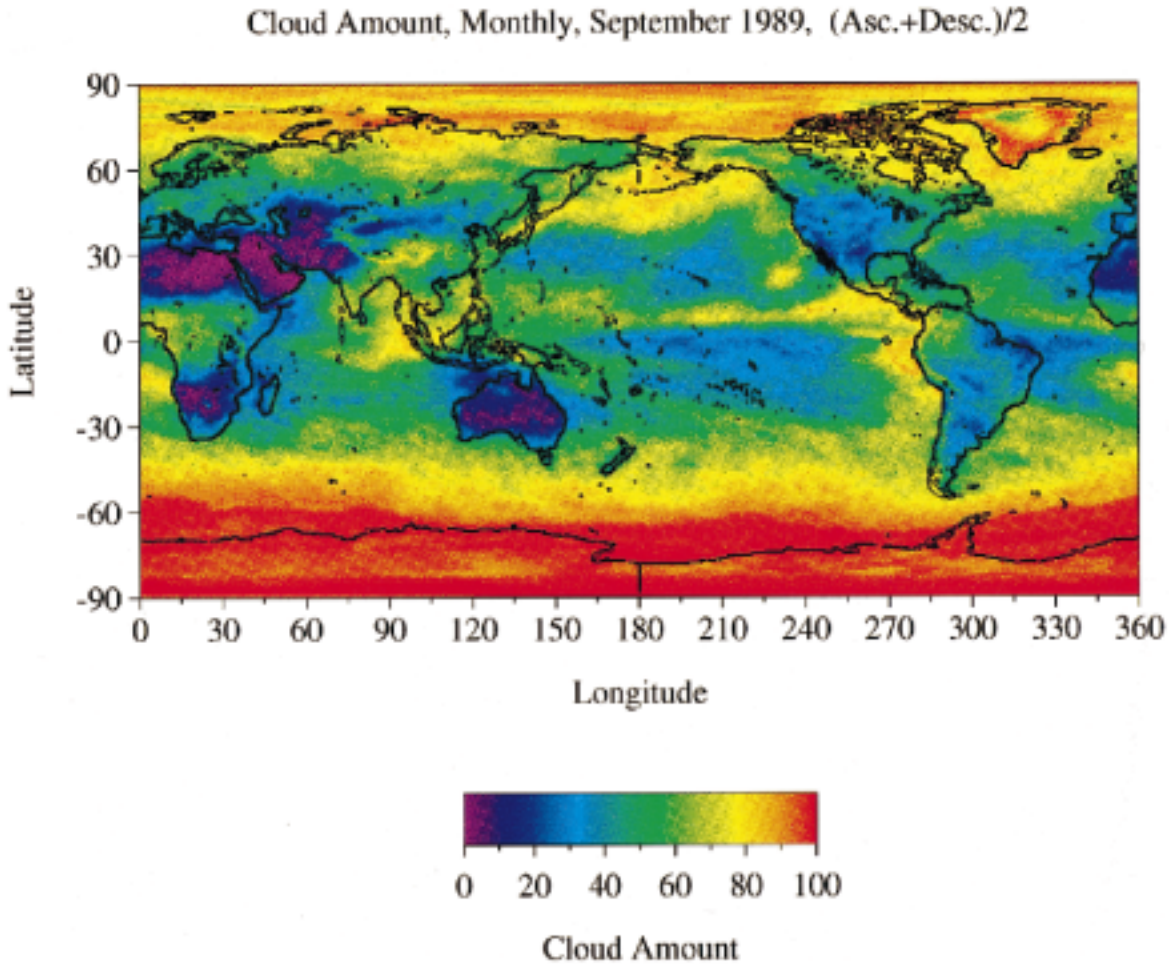

FIG. 8. Map of CLAVR-1 monthly mean total cloud amount (SESC method) for September 1989 averaged for ascending (mostly daytime) and descending (mostly nighttime) orbital passes. Resolution is 1° lat and long.

submitted to *J. Atmos. Oceanic Technol.*). The spatial distribution of cloud cover is consistent with two other global satellite climatologies: ISCCP, Rossow et al. (1993); and *Nimbus-7,* Stowe et al. (1989). In general, cloud cover is less than 30% over desert regions, 20%–50% over subtropical anticyclonic circulation regions, and 50%–80% in the midlatitude storm tracks and the intertropical convergence zone. CLAVR-1 has significantly more cloud cover than either of the other climatologies near the poles with values between 80% and 100%. One known cause for CLAVR-1 to overestimate cloud cover in the poles results from the difference in snow/ice emissivity as a function of view angle between channels 4 and 5. The FMFT is used to restore cold pixels to RESTORED-CLEAR in the nighttime algorithm, and because of these emissivity effects, fails to restore these cold pixels to RESTORED-CLEAR when viewing snow or ice. The CLAVR-2 algorithm has removed this overestimate by implementing an FMFT threshold, which is a function of view angle (Davis et al. 1999, manuscript submitted to *J. Atmos. Oceanic Technol.*).

6. Discussion and concluding remarks

The bases of cloud detection with multispectral imager data have been discussed, and their application to global AVHRR data by means of a cloud classification algorithm (viz., CLAVR-1) has been elaborated. Theoretical and empirical evidence has been presented to support the specifics of the algorithm. The algorithm has been evaluated by computer-enhanced image analysis of segments of orbital data, as well as by statistical comparisons of derived total cloud amount with an analyst's interpretation of these images. Intercomparisons of total cloud amount at the mapped grid resolution with other global cloud datasets have been published elsewhere (Hou et al. 1993) and will be the subject of future publications.

Although the nighttime land algorithm works quite

well during the summer and in the subtropics and Tropics at all seasons, its performance degrades at middle and high latitudes, particularly in the winter season and in mountainous terrain. The land surface, especially when snow covered, can become very cold at night, sometimes colder than the tops of the overlying clouds. In irregular terrain, especially in light winds, nocturnal temperature inversions are prevalent and surface temperature variability is often large. The algorithm for nighttime ocean scenes is simpler than the one for daytime scenes over land or ocean (e.g., only one restoral test is employed). Nevertheless, the nighttime algorithm appears to work rather well. Admittedly, its validation cannot be as reliable as that for the daytime algorithm because imagery is restricted to the three infrared channels.

Generally, the CLAVR-1 fractional cloud amounts computed by assigning 50% cloud cover to MIXED pixel arrays (FFS method) appear to be overestimated by about 0.10 when cloud amount is small and underestimated by about the same when cloud amount is large when compared with an analyst's interpretation of visible and infrared images. Use of the SESC method, where the fractional cover of MIXED pixels is computed explicitly, reduces this bias to about 0.05 for the locations and dates studied. However, for certain geographical locations and seasons, larger errors have been observed. These result from a) latitude/longitude boundaries affecting the cloud test sequence (see flowcharts in the appendix); b) radiative similarities between cloud-free ocean, sun-glint, low stratiform clouds; c) departure of land and snow/ice infrared emissivity from unity; and d) at latitudes greater than 50° over ocean, some clouds are identified as sea ice. These problems are being addressed in Davis et al. (1999, manuscript submitted to *J. Atmos. Oceanic Technol.*) and Vemury et al. (1999, manuscript submitted to *J. Atmos. Oceanic Technol.*).

Subsequent CLAVR algorithms (2 and 3), nearing completion should improve upon the quality of CLOUD/CLEAR classifications and will separate total cloud into amounts for different cloud types. New features include providing pixel-scale cloud classifications, gridded cloud amount by layered types (liquid phase, mixed phase, thick glaciated opaque, and semitransparent ice) and maintaining the quality and increasing the quantity of pixel-level CLEAR classifications through the use of dynamic cloud/no-cloud threshold tests. These modifications also include a land surface–type classification database, snow/ice databases, and an improved cloud test algorithm at polar latitudes.

Although not perfect, the results presented show that the CLAVR-1 classifications and cloud amounts are sufficiently accurate to justify testing their use in generating other climate parameters such as vegetation index, sea and earth surface temperature and albedo, and atmospheric aerosol concentration over the oceans. The CLOUDY and CLEAR pixel radiances can be used to estimate earth radiation budget, cloud and aerosol parameters, and their radiative forcing. The initial effort to do this is the AVHRR Pathfinder Atmosphere project (UCAR 1994). It uses cloud classified radiances and total cloud amount from CLAVR-1 to compute estimates of broadband radiation budget parameters at the top of the atmosphere for ''all'' and ''clear-sky'' conditions and aerosol optical thickness over the oceans. This is done on a daily, pentad, and monthly basis, and on a 110-km equal-area global grid for all NOAA afternoon satellites since *NOAA-7*, which was launched in 1981. This Pathfinder dataset, currently 16 years in extent, can be accessed electronically (ftp://aries.nesdis.noaa.gov; http://las.saa.noaa.gov). A paper is in preparation that evaluates the dataset quality and its usefulness for addressing climate change questions.

Acknowledgments. The authors are indebted to the following individual scientists and computer analysts who have used their skills and knowledge working on various parts of this project since its inception in 1988: P. Pellegrino, R. Carey, G. Gutman, C. Long, C. Duda, C. Watkins, and K. Campana of NOAA; and S. Hart, G. Major, D. Carr, C. Praderas, R. Yanamandra, L. Lu, B. Zhang, D. Moore, Y. Hou, S. Vemury, R. Anne, D. Love, G. Luo, F. Jing of various contracting companies. We are also appreciative of the assistance given by management in NOAA, particularly G. Ohring, A. Gruber, H. Jacobowitz, and D. Tarpley of the Office of Research and Applications, and to W. Murray, of the NOAA/Office of Global Programs. Funding for this work was provided by these two offices in support of new product development objectives in NESDIS and the NOAA Climate and Global Change Program objectives.

APPENDIX

Algorithm Description

This appendix presents flowcharts to aid in understanding the CLAVR-1 algorithm described in section 4. The theoretical basis for detection of thin cirrus and low stratus clouds with spectral signature tests is given. The spacecraft-dependent coefficients for the channel-3 albedo computation discussed in section 3a are provided. Also, details of developing thresholds for the nighttime spectral signature tests (viz., the ULST, FMFT, and CIRT) that are functionally dependent upon the channel-4 brightness temperature are presented. Finally, the equation for the gamma angle test used to treat specular reflection conditions is defined, as are some details of the RESTORED-CLEAR process.

a. Decision-tree flow charts

Flowcharts of the CLAVR-1 algorithm, as described in section 4, are presented in Figs. A1–A4. They show all the paths that could be taken by a 2 pixel × 2 scanline (4-pixel) array of AVHRR data. They also show the

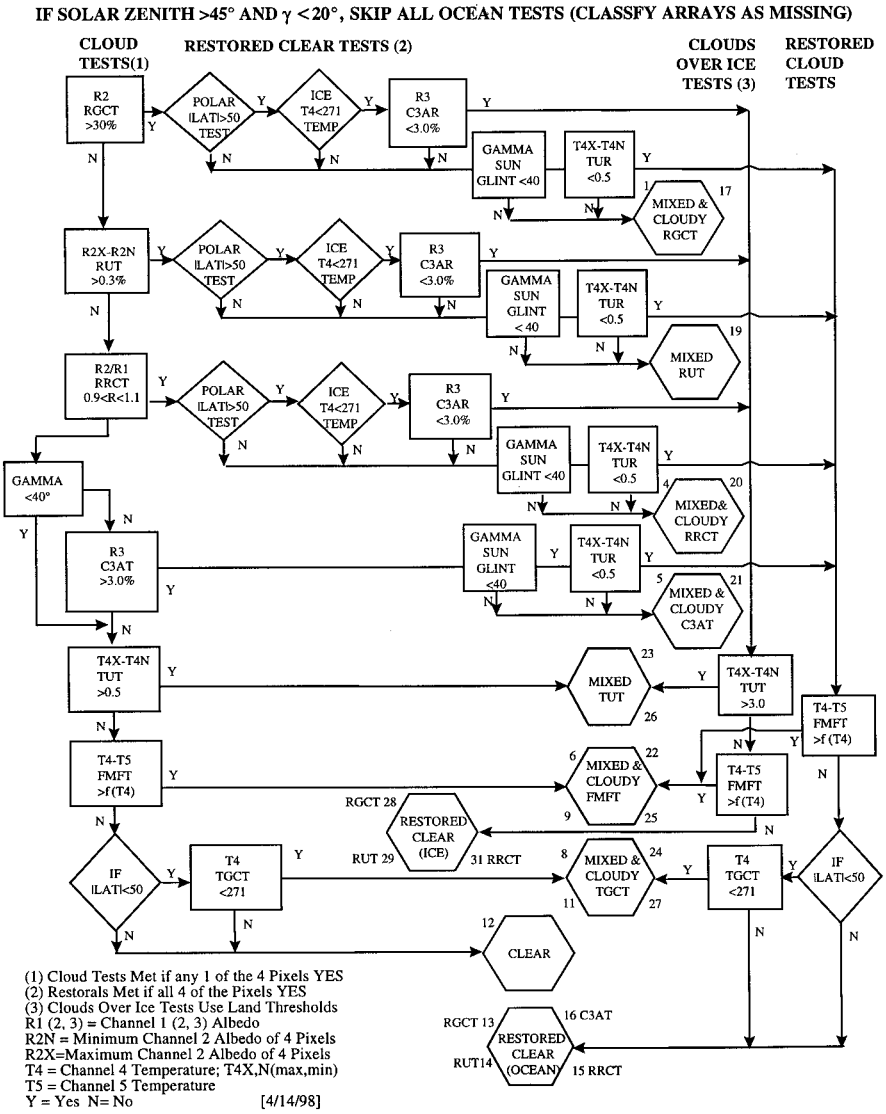

FIG. A1. Logical flowchart for daytime/ocean algorithm of CLAVR-1 code.

channel used, the name of the test, any special condition, and the cloud code used to represent the path taken. Square boxes represent threshold tests, diamonds represent special conditions for the tests, and hexagonal boxes represent the final classification categories. The numbers at the corners of the hexagonal boxes represent the cloud code that is unique to the path taken: upper-left corner, CLOUDY upper-right corner, MIXED; lower-left corner, CLOUDY after being RESTORED-CLEAR; lower-right corner, MIXED after being RESTORED-CLEAR.

The algorithm is different when viewing land or ocean and when viewing by day or by night. CLAVR-1 uses a land/sea auxiliary database with an equal-angle grid resolution of $\frac{1}{16}^\circ$ (approximately 7 km at the equator) to specify what type of surface is being viewed in a given pixel. If three or more of the pixels in an array are over land, the array is classified as land, otherwise it is classified as ocean or inland water surface. Certain tests are suspended over desert areas, which are approximated by rectangular latitude/longitude regions defined from Mathews (1985): Africa (land between 10°–35°N, 20°W–30°E); Saudi Arabia–western Asia (land between 5°–50°N, 30°–60°E); central Asia (25°–50°N, 60°–110°E); and Australia (19°–31°S, 121°–141°E).

b. Cloud radiative-transfer model

For three of the nighttime tests, one of which is also a daytime test (the FMFT), a simple cloud radiative-transfer model adapted from Smith et al. (1974) is used to demonstrate how the brightness temperature differences between pairs of AVHRR channels vary with

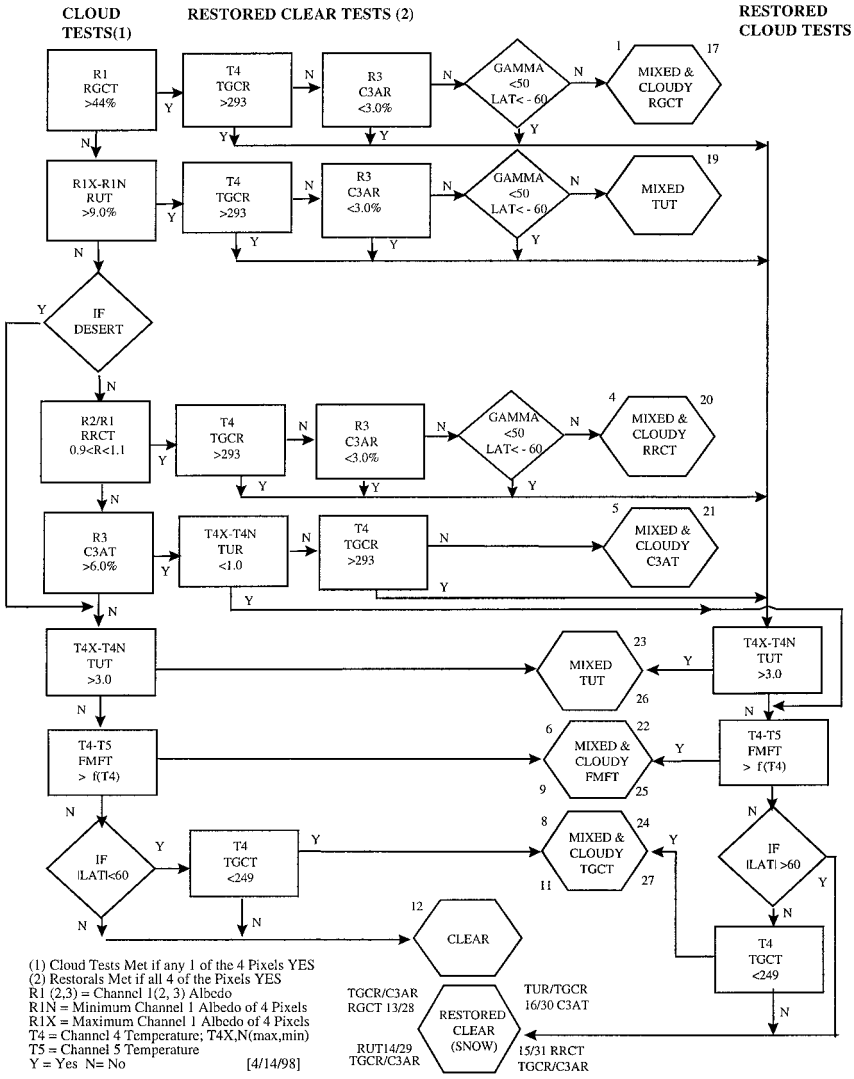

FIG. A2. Same as Fig. A1 but for the daytime/land algorithm.

cloud optical thickness (δ_c) under several combinations of atmospheric and cloud conditions.

The cloud radiance model is as follows:

$$I = [\rho_s + N(\rho_c - \rho_s)]F + [(\tau_c - 1)N + 1]\epsilon_s B_s + N\epsilon_c B_c. \quad \text{(A1)}$$

Here N is the fractional cloud amount, and the model makes use of the conservation of energy principle requiring that the bulk reflectivity (ρ_c), emissivity (ϵ_c), and transmissivity (τ_c) of a cloud sum to 1.0. Values of these optical properties for wavelengths approximately at the center of the three thermal channels of the AVHRR were taken from Hunt (1973) over a range of δ_c for several cloud water droplet or ice particle radii (R_d). Here we have used an optical thickness that is wavelength independent since, for a given δ_c, the other optical properties of the cloud in Eq. (A1) do allow for significant variations among 3.7, 10.8, and 11.9 μm.

Restricting the study to cloud-filled pixels ($N = 1.0$) over an ocean at night fixes the optical properties of the surface ($\rho_s = 0.007$, $\epsilon_s = 0.993$, $\tau_s = 0$) and eliminates solar radiation ($F = 0$). The temperature of the surface (T_s) and the cloud (T_c) are converted to Planck radiances (B_s, B_c). Here T_s is the cloud-free brightness temperature, which includes atmospheric attenuation unless ''dry'' is specified, in which case it is the physical surface temperature. Then, after supplying the optical properties corresponding to δ_c values ranging from 0.01 (nearly transparent cloud) to 10.0 (virtually opaque cloud) or greater, for two water droplet sizes (5 and 10 μm) and three ice particle sizes (20, 40, and 100 μm), the model output consists of the Planck radiances (I) corresponding to the central wavenumbers of channels 3, 4, and 5. The final step is to convert these Planck radiances to the corresponding channel 3, 4, and 5 brightness temperatures (T_3, T_4, and T_5).

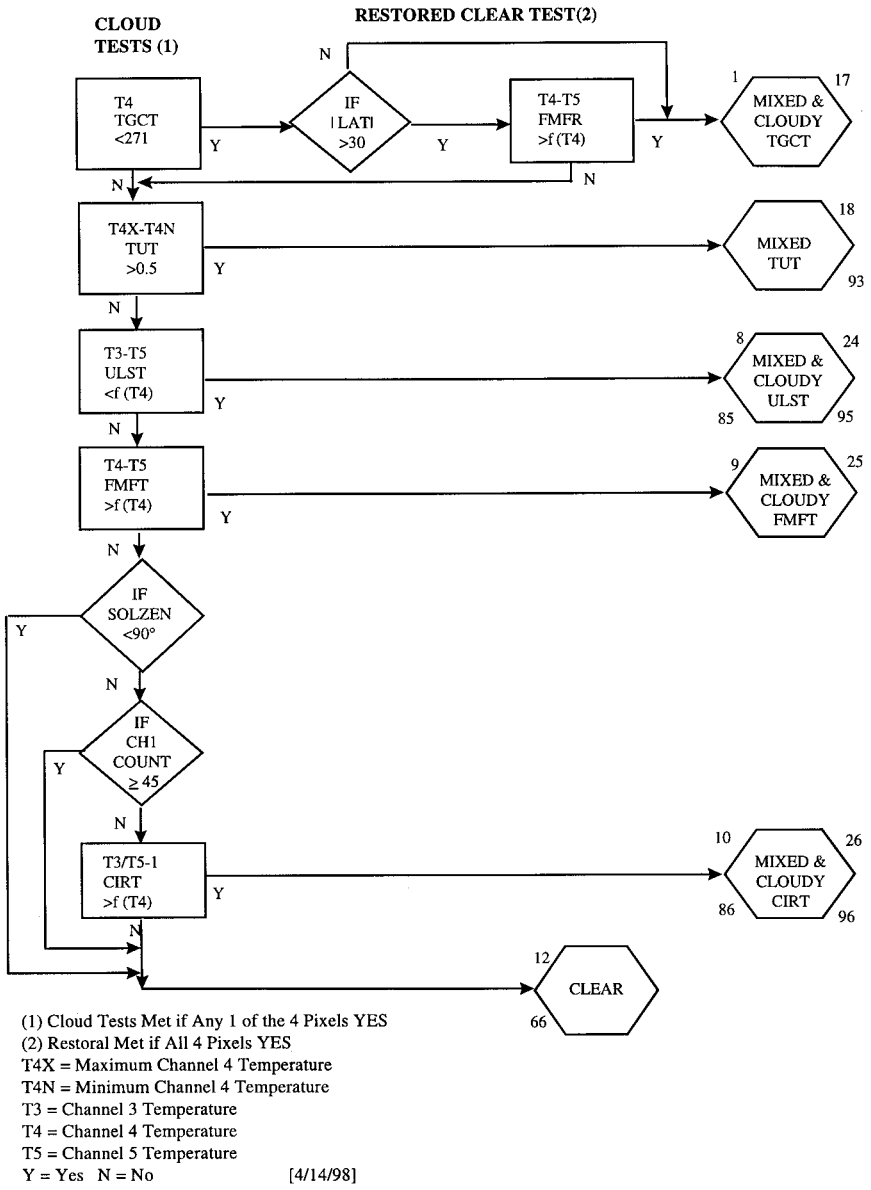

FIG. A3. Same as Fig. A1 but for the nighttime/ocean algorithm.

Figure A5 gives graphs of $T_3 - T_5$ for a dry subtropical/midlatitude atmosphere with $T_s = 292$ K. Water particles having $R_d = 5$ and 10 μm are in Figs. A5a–A5c for $T_c = 286$, 276, and 256 K, respectively. The graphs clearly show how all the clouds are associated with substantially negative values of $(T_3 - T_5)$ when they are sufficiently opaque, particularly the lowest (warmest) clouds having small water droplets. This is the basis of the ULST test at night. Clouds with larger water droplets show the same effects as clouds with smaller droplets, but the variation with δ_c is reduced. All but the warmest clouds also show a distinct positive peak in $(T_3 - T_5)$ for relatively thin clouds (at $\delta_c = 1$). Thus, although the quantity $(T_3 - T_5)$ has been used chiefly for a ULST (opaque low clouds), it appears from these diagrams that it could also be useful for low/middle or middle clouds: the opaque ones having $\delta_c > 10$ behave like low clouds, whereas the thin ones ($\delta_c = 1.0$) behave like cirrus clouds. For comparison purposes, an ice cloud at $T_c = 236$ K with $R_d = 20$ and 40 μm is shown in Fig. A5d. As discussed in the text, this is the basis for the use of these two channels for cirrus detection at night.

Similar results are obtained for $T_4 - T_5$, but this has been well documented by others (Prabhakara et al. 1988; Inoue 1985).

c. Calculation of the channel-3 albedo

The channel-3 albedo test (C3AT) first requires obtaining the channel-3 albedo (C3A) using the following equations:

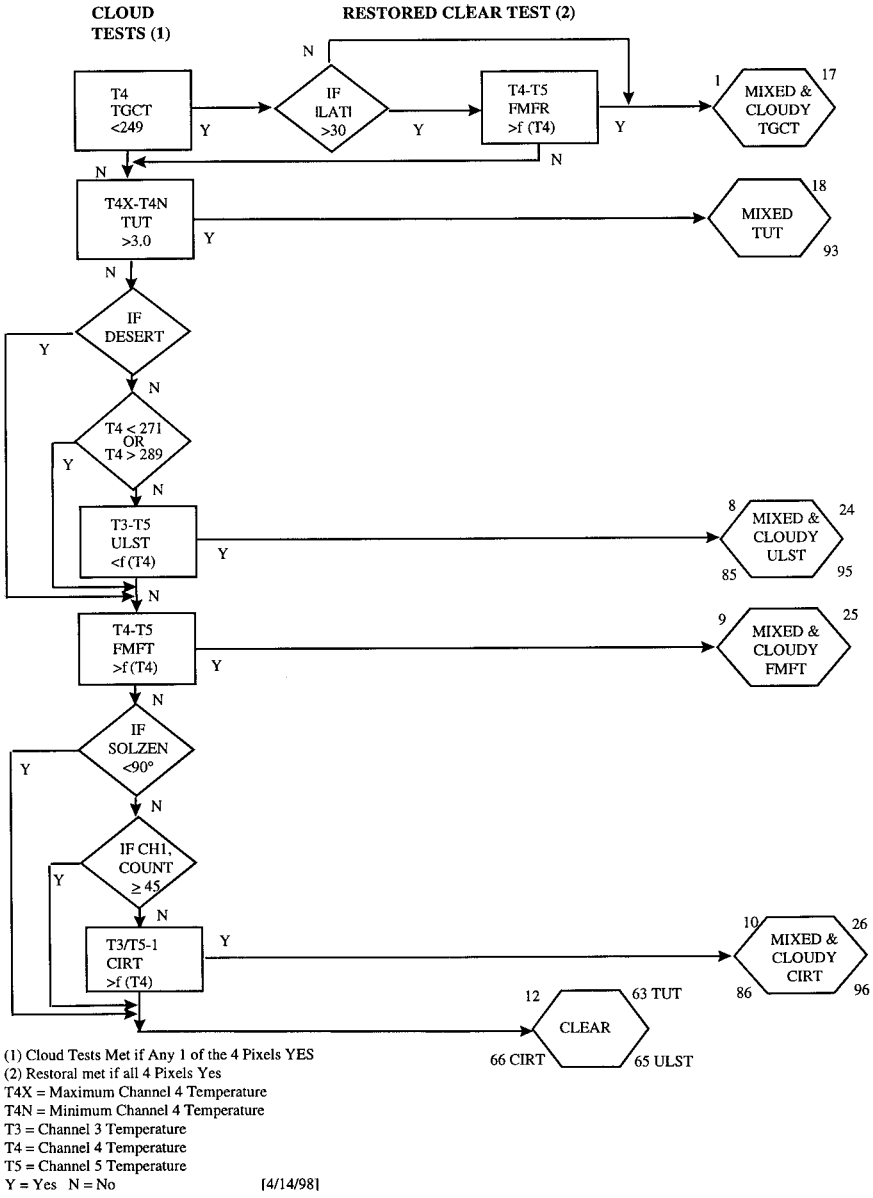

FIG. A4. Same as Fig. A1 but for the nighttime/land algorithm.

$$\mathrm{C3A} = 3.14159\Delta R_3 \cdot 100\% \div [\cos(Z_o)(D_o/D)^2 S_3], \quad \text{(A2a)}$$

$$\mathrm{delR}_3 = B(T_3) - B(T_{3e}), \quad \text{(A2b)}$$

$$T_{3e} = -[(b/a)T_4 + (c/a)T_5 + d/a]. \quad \text{(A2c)}$$

The variables in the above three equations are spacecraft dependent and are given in Table A1 for the satellites where the CLAVR algorithm has been applied. In the above, ΔR_3 is the estimated reflected radiance, S_3 is the channel-3 filtered solar irradiance at normal incidence- and mean Earth–sun distance, Z_o is solar zenith angle, (D_o/D) is the ratio of mean to actual Earth–sun distance, B is the Planck function at the channel-3 central wavenumber ν_o, T_i is the observed equivalent blackbody temperature in Ch(i), and T_{3e} is the estimated brightness temperature for channel 3 due to emission only. The constants in Eq. (A2c) are derived from empirical relationships for cloud-free sea surface conditions that account for the attenuating effects of variable atmospheric-column water vapor amounts (McClain et al. 1985).

d. Establishment of temperature-dependent thresholds

The spectral-signature cloud tests, namely, FMFT, ULST, and CIRT (see section 3b), use thresholds that are dependent on T_4 to implicitly account for differences

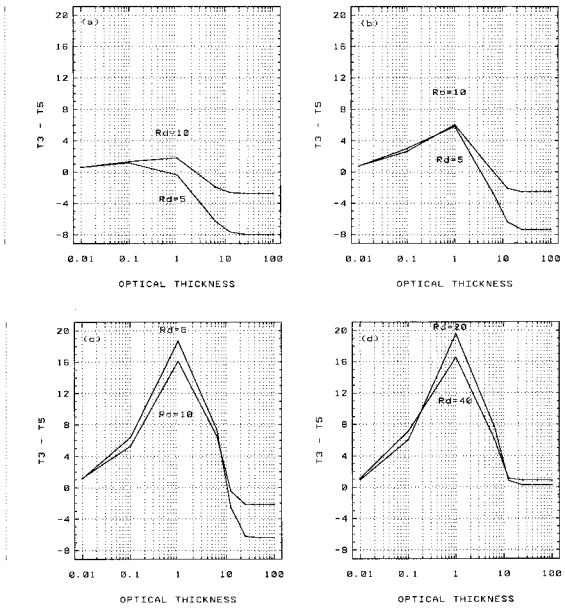

FIG. A5. Theoretical relationship of difference in brightness temperature between channels 3 and 5 of AVHRR to the cloud optical thickness δ_c for different cloud particle radii R_d, and cloud-top temperatures T_c: (a) $T_c = 286$ K, (b) $T_c = 276$ K, (c) $T_c = 256$ K, and (d) $T_c = 236$ K. The radiative transfer computations [Eqn. (A1)] were done for a midlatitude atmosphere without water vapor and at night with $T_s = 292$ K. The droplets were assumed to be water in all but the last panel, where ice was assumed.

in water vapor absorption. They have been derived using 1200 globally distributed cloud-free atmospheric soundings (905 for land and 295 for maritime stations) in a radiative-transfer model (Weinreb and Hill 1980) to generate a simulation database of calculated T_3, T_4, and T_5 brightness temperatures, accounting for each channel's spectral response function. These thresholds have not been derived for each spacecraft, as it appeared from empirical studies that their application as cloud/no-cloud classifiers did not require that degree of precision. The total number of points is actually triple the above numbers because brightness temperatures were computed for three values of satellite zenith angle: satellite zenith angle = 0°, 30°, and 60°. These results were used to plot Figs. 1–3 in section 3b.

The T_4-dependent FMFT ocean and land thresholds were defined by fitting fourth- or fifth-degree polynomials in T_4 to the maximum values of FMF for these cloud-free conditions. The simulation database was supplemented over land with some AVHRR data from daytime deserts to cover the observed dynamic range of the T_4 measurements, including the effects of skin-shelter temperature discontinuities that are not in the simulation database. The threshold has the following form:

$$\text{FMFT threshold} = \sum \{a_i T_4^i\} \qquad i = 0\text{–}4 \text{ or } 5, \quad \text{(A3a)}$$

where Table A2 gives the sets of coefficients. The FMFT threshold equation for the ocean is applied when 240 K $< T_4 <$ 287 K. When $T_4 <$ 240 K, the threshold is set to zero. If $T_4 >$ 295 K, it is set to 4.0 K. When 287 K $< T_4 <$ 295 K, the following linear relation is used:

$$\text{FMFT threshold} = 0.154(T_4 - 287) + 2.77. \quad \text{(A3b)}$$

For land surfaces, the FMFT threshold equation is applied in the T_4 range from 260 to 305 K. If $T_4 <$ 260 K, the threshold is set to zero, and if $T_4 >$ 305 K, it is set to 7.8 K, a number resulting from the inclusion of desert observations from AVHRR. When land surface temperatures become so high during daytime that channels 4 and/or 5 approach saturation values (viz., at and above about 315 K), the FMFT is suspended.

The ULST, based on channels 3–5 temperature difference ($T_3 - T_5$), is an important spectral signature test used in the MCSST nighttime algorithm to detect low stratus clouds (McClain et al. 1985). An exponential curve was fit to the middle of the sample of points to define the ULST threshold as follows:

$$\text{ULST threshold} = \exp(a + bT_4) - 1.0, \quad \text{(A4)}$$

where $a = -9.375$, $b = 0.0342$, and the threshold varies from 0.0 to +1.4 as T_4 varies from 273 to 300 K. Over land, ULST is not applied if $T_4 <$ 271 K (lower limit of experience with ULST over oceans) or $T_4 >$ 289 K [maximum zonally averaged, low-cloud temperature over land at night from Stowe et al. (1989)]. In addition to this temperature restriction, it was found empirically that the constant (−1) used in Eq. (A4) needs to be lowered to −3.0 to account for land surface emissivities

TABLE A2. Coefficients for FMFT threshold equations.

FMFT coefficients	FMFT–ocean	FMFT–land
a_0	9.27066E+04*	−1.34436E+04
a_1	−1.79203E+03	1.94945E+02
a_2	1.38305E+01	−1.05635E+00
a_3	−5.32679E−02	2.53361E−03
a_4	1.02374E−04	−2.26786E−06
a_5	−7.85333E−08	0.0

* Read notation as 9.27066×10^4, for example.

TABLE A1. Spacecraft-dependent coefficients for Channel 3 albedo computation.

Spacecraft	S_3	ν_o	a	b	c	d
NOAA-7	16.0872	2671.26	1.000000	−2.535500	1.56201	−6.71000
NOAA-9	16.1510	2677.68	0.982490	−2.659000	1.68550	−1.25000
NOAA-11	16.0707	2670.95	0.962422	−2.127852	1.16516	−0.74400
NOAA-14	15.8066	2645.90	1.000000	−2.915924	1.92754	−1.21284

less than unity at wavelengths near 3.7 μm (Hovis 1966).

The CIRT is defined as $(T_3 - T_5)/T_5$ and is shown in Fig. 3. Although there are a few outliers present and the sampling is probably inadequate for the warmest and wettest air masses, one can reasonably define an upper limit, that is, maximum CIRT, as a function of T_4. That upper limit has been chosen for the CIRT threshold and is approximately represented for three ranges of temperature as follows:

$$T_4 < 273\ \text{K}: \quad \text{CIRT threshold} = 0.00,$$

$$273 < T_4 < 292\ \text{K}: \quad \text{CIRT threshold} = 1.77467(10^{-3})T_4 - 0.485328,$$

and

$$T_4 > 292\ \text{K}: \quad \text{CIRT threshold} = 0.033. \qquad \text{(A5)}$$

Problems can be encountered with tests involving channel 3 (ocean or land) if electrical interference ''noise,'' which has been present to a greater or lesser extent with this AVHRR channel on all the NOAA satellites to date, becomes too large (Warren 1989). Furthermore, it should be noted that channel-3 brightness temperatures become unreliable when they are lower than about 240 K.

e. Gamma equation (defining cone of specular reflection)

The restoral tests over ocean and Antarctica described in section 4 are applied when viewing within a specified angular distance from the specular reflection direction for a plane ocean surface. The half-angle of this cone, gamma, is defined as

$$\text{gamma} = \cos^{-1}[\cos(Z_o)\cos(Z) + \sin(Z_o)\sin(Z)\cos(A)], \qquad \text{(A6)}$$

where Z_o and Z are solar and satellite zenith angles, respectively, and A is relative azimuth angle ($A < 90°$ viewing toward the specular ray, $A > 90°$ viewing away from it).

f. Some details of the daytime RESTORED-CLEAR process

With reference to Figs. A1 and A2, a threshold of 3% is chosen for the daytime channel-3 albedo restoral (C3AR) test; this is slightly above the reflectances of snow and sea ice reported in Warren (1984). All four pixels in the 2×2 array must be less than this threshold for the array to be classified RESTORED-CLEAR. Over oceans, the C3AR test is restricted to cold polar regions, as sea ice tests are not necessary at other latitudes. Over land there is no such restriction, but the C3AR is skipped at latitudes poleward of 60°S when viewing in a direction where specular reflection from Antarctic snow elevates this channel's reflectance above the threshold. This direction is determined by the gamma angle (see section A5). In this case, gamma $<50°$ is used.

Pixels passing the daytime reflectance-based cloud tests over desert and other arid land types are subjected to a TGCT where the threshold is the temperature of the maximum zonally averaged low-cloud temperature observed over sunlit land in the *Nimbus-7* cloud climatology [viz., 293 K—i.e., above the temperature of the warmest cloud observed by *Nimbus-7* (Stowe et al. 1989)]. Any MIXED or CLOUDY array where all four pixels have T_4 greater than this threshold are classified RESTORED-CLEAR by this TGCR test. Because some nondesert land surfaces exhibit channel 3 albedos greater than the 6% C3AT threshold, pixels passing this test are subjected to a TUR test before the TGCR test is invoked. The TUR threshold is set empirically to 1.0 K—using case studies, it was found unlikely that a cloud would be this thermally uniform over daytime land areas.

Because of sun glint, a TUR test (in this case using a limit of <0.5 K) is applied only when the satellite is viewing within the expected region of solar specular reflection defined by the gamma angle. Except for the very end of each satellite's lifetime, where it has drifted to late afternoon local observation times, a gamma angle of 40° should define the angular space where most of this specular reflection ambiguity occurs. The channel-3 albedo is so sensitive to specular reflection, however, that the C3AT is bipassed when gamma less than 40° (see Fig. A1). For the late afternoon orbits, specular reflection can be so intense when solar zenith angles exceed 45° and gamma $<20°$ that the CLAVR-1 algorithm requires that all tests be bypassed (i.e., pixels treated as missing) in this geometrically defined zone. This removes a high bias in cloud amount that results from CLEAR ocean pixels erroneously being called CLOUDY as the satellite progressively ages.

The specular reflection test assumes that clouds will have a stronger spatial signature than the cloud-free ocean in the infrared when viewing in the specular direction. However, some low stratus clouds can satisfy the thermal restoral test (viz., TUR), that is, be thermally uniform to less than 0.5 K. Thus, to avoid misclassification errors when processing the CLAVR-1 datasets, we have learned to handle certain situations as follows: 1) treat Restored-CLEAR arrays passing the RGCT over ocean (cloud code identifies path) as CLOUDY (the RGCT threshold is much brighter than most specular reflection regions); and 2) treat pixels subjected to either of the next two reflectance tests in the daytime ocean sequence (RUT or RRCT), when RESTORED-CLEAR, as missing. Even with the foregoing restrictions, it is still possible to classify pixel arrays as CLEAR in the region of specular reflection (see Vemury et al. 1999, manuscript submitted to *J. Atmos. Oceanic Technol*).

REFERENCES

Ardanuy, P. E., L. L. Stowe, A. Gruber, and M. Weiss, 1991: Shortwave, longwave, and net cloud-radiative forcing as determined from *Nimbus-7* observations. *J. Geophys. Res.,* **96,** 18 537–18 549.

Baum, B. A., B. A. Wielicki, and P. Minnis, 1992: Cloud-property retrieval using merged HIRS and AVHRR data. *J. Appl. Meteor.,* **31,** 351–369.

Cess, R. D., and Coauthors, 1989: Interpretation of cloud-climate feedback as produced by 14 atmospheric general circulation models. *Science,* **245,** 513–516.

Coakley, J. A., and F. P. Bretherton, 1982: Cloud cover from high-resolution scanner data: Detecting and allowing for partially filled fields of view. *J. Geophys. Res.,* **87,** 4917–4932.

Davis, P. D., G. Majors, and H. Jacobowitz, 1984: An assessment of *Nimbus-7* Earth Radiation Budget shortwave scanner data by correlative analysis with narrow-band CZCS data. *J. Geophys. Res.,* **89,** 5077–5088.

Deirmendjian, D., 1969: *Electromagnetic Scattering on Spherical Polydispersions.* Elsevier, 290 pp.

Dozier, J., and S. G. Warren, 1982: Effect of viewing angle on the infrared brightness temperature of snow. *Water Resour. Res.,* **19** (5), 1424–1434.

Gutman, G. G., 1992: Satellite daytime image classification for global studies of Earth's surface parameters from polar orbiters. *Int. J. Remote Sens.,* **13,** 209–234.

——, D. Tarpley, A. Ignatov, and S. Olson, 1995: The enhanced NOAA global land dataset from the Advanced Very High Resolution Radiometer. *Bull. Amer. Meteor. Soc.,* **76,** 1141–1156.

Hamill, T. M., R. P. d'Entremont, and J. T. Bunting, 1992: A description of the Air Force Real-Time Nephanalysis Model. *Wea. Forecasting,* **7,** 288–306.

Hou, Y.-T., K. A. Campana, K. E. Mitchell, S.-K. Yang, and L. L. Stowe, 1993: Comparison of an experimental NOAA AVHRR cloud dataset with other observed and forecast cloud datasets. *J. Atmos. Oceanic Technol.,* **10,** 833–848.

Hovis, W. A., Jr., 1966: Infrared spectral reflectance of some common minerals. *Appl. Opt.,* **5,** 245–248.

Hunt, G. E., 1973: Radiative properties of terrestrial clouds at visible and infrared thermal window wavelengths. *Quart. J. Roy. Meteor. Soc.,* **99,** 346–369.

Inoue, T., 1985: On the temperature and effective emissivity determination of semi-transparent clouds by bi-spectral measurements in the 10 micron window region. *J. Meteor. Soc. Japan,* **63** (1), 88–89.

Kidwell, K. B., Ed., 1991: NOAA polar orbiter data user's guide. NOAA National Environmental Satellite Data and Information Service, 120 pp. [Available from 151 Patton Ave., Asheville, NC 28801-5001.]

King, M. D., Y. J. Kaufman, W. P. Menzel, and D. Tanre, 1992: Remote sensing of cloud, aerosol, and water vapor properties from the Moderate Resolution Imaging Spectrometer (MODIS). *IEEE Trans. Geosci. Remote. Sens.,* **30** (1), 2–15.

Luo, G., P. A. Davis, L. L. Stowe, and E. P. McClain, 1995: A pixel-scale algorithm of cloud type, layer, and amount for AVHRR data. Part I: Nighttime. *J. Atmos. Oceanic Technol.,* **12,** 1013–1037.

Mathews, E., 1985: Atlas of archived vegetation, land-use and seasonal albedo data sets. NASA Tech. Memo. 86199, Goddard Institute for Space Studies, New York, NY, 54 pp. [Available from Goddard Institute for Space Studies, 2880 Broadway, New York, NY 10025.]

McClain, E. P., 1989: Global sea surface temperatures and cloud clearing for aerosol optical depth estimates. *Int. J. Remote Sens.,* **10,** 763–769.

——, W. G. Pichel, and C. C. Walton, 1985: Comparative performance of AVHRR-based multichannel sea surface temperatures. *J. Geophys. Res.,* **90** (C6), 11 587–11 601.

Mokhov, I. I., and M. E. Schlesinger, 1993: Analysis of global cloudiness. 1: Comparison of Meteor, *Nimbus-7,* and International Satellite Cloud Climatology Project (ISCCP) satellite data. *J. Geophys. Res.,* **98,** 12 849–12 868.

——, and ——, 1994: Analysis of global cloudiness. Part 2: Comparison of ground-based and satellite-based cloud climatologies. *J. Geophys. Res.,* **99,** 17 045–17 065.

Molnar, G., and J. A. Coakley Jr., 1985: Retrieval of cloud cover from satellite imagery data: A statistical approach. *J. Geophys. Res.,* **90** (D7), 12 960–12 970.

Nakajima, T., and M. King, 1990: Determination of the optical thickness and effective particle radius of clouds from reflected solar radiation measurements. Part I: Theory. *J. Atmos. Sci.,* **47,** 1878–1893.

Prabhakara, C., R. S. Fraser, G. Dalu, M. C. Wu, and R. J. Curran, 1988: Thin cirrus clouds: Seasonal distribution over oceans deduced from *Nimbus-4* IRIS. *J. Appl. Meteor.,* **27,** 379–399.

Rao, C. R. N., and J. Chen, 1995: Inter-satellite calibration linkages for the visible and near infrared channels of the Advanced Very High Resolution Radiometer on *NOAA-7, -9,* and *-11* spacecraft. *Int. J. Remote Sens.,* **16,** 1931–1942.

Rossow, W. B., and L. C. Garder, 1993: Cloud detection using satellite measurements of infrared and visible radiances for ISCCP. *J. Climate,* **6,** 2341–2369.

——, A. W. Walker, and L. C. Garder, 1993: Comparison of ISCCP and other cloud amounts. *J. Climate,* **6,** 2394–2418.

Saunders, R. W., and K. T. Kriebel, 1988: An improved method for detecting clear sky and cloudy radiances from AVHRR data. *Int. J. Remote Sens.,* **9,** 123–150.

Schiffer, R. A., and W. B. Rossow, 1983: The International Satellite Cloud Climatology Program (ISCCP): The first project of the World Climate Research Program. *Bull. Amer. Meteor. Soc.,* **64,** 779–784.

Slingo, A., 1990: Sensitivity of Earth radiation budget to changes in low clouds. *Nature,* **343,** 49–51.

Smith, W. L., H. M. Woolf, P. G. Abel, C. M. Hayden, M. Chalfant, and N. Grody, 1974: *Nimbus-5* Sounder Data Processing System Part I: Measurement characteristics and data reduction procedures. NOAA Tech. Memo. NESS 57, U. S. Department of Commerce, Washington, DC, 99 pp. [Available from 5200 Auth Rd., Rm 703, Camp Springs, MD 20746.]

Stowe, L. L., 1984: Evaluation of *Nimbus-7* THIR/CLE and Air Force three-dimensional nephanalysis estimates of cloud amount. *J. Geophys. Res.,* **89** (D4), 5370–5380.

——, 1991: Cloud and aerosol products at NOAA/NESDIS. *Palaeogeogr. Palaeoclimatol. Palaeoecol.,* **90,** 25–32.

——, and Coauthors, 1989: *Nimbus-7* global cloud climatology. Part II: First year results. *J. Climate,* **2,** 671–709.

——, E. P. McClain, R. Carey, P. Pellegrino, G. Gutman, P. Davis, C. Long, and S. Hart, 1991: Global distribution of cloud cover derived from NOAA/AVHRR operational satellite data. *Adv. Space Res.,* **11,** 51–54.

——, S. K. Vemury, and A. V. Rao, 1993: AVHRR clear-sky radiation data sets at NOAA/NESDIS. *Adv. Space Res.,* **14,** 113–116.

——, P. A. Davis, and E. P. McClain, 1995: Evaluating the CLAVR (Clouds from AVHRR) Phase I cloud cover experimental product. *Adv. Space Res.,* **16,** 21–24.

——, A. M. Ignatov, and R. R. Singh, 1997: Development, validation, and potential enhancements to the second generation operational aerosol product at NOAA/NESDIS. *J. Geophys. Res.,* **102** (D14), 16 923–16 934.

Tarpley, J. D., S. R. Schneider, and R. L. Money, 1984: Global vegetation indices from the *NOAA-7* meteorological satellite. *J. Climate Appl. Meteor.,* **23,** 491–494.

UCAR, 1994: The NOAA–NASA pathfinder program. The University Corporation for Atmospheric Research, Boulder, Colorado, 22 pp.

Uddstrom, M. J., and W. R. Gray, 1996: Satellite cloud classification and rain-rate estimation using multi-spectral radiances and measures of spatial texture. *J. Appl. Meteor.,* **35,** 839–858.

Warren, D., 1989: AVHRR channel-3 noise and methods for its removal. *Int. J. Remote Sens.,* **4,5,** 645–651.

Warren, S. G., 1984: Optical constants of ice from the ultraviolet to the microwave. *Appl. Opt.*, **23,** 1206–1225.

——, C. J. Hahn, J. London, R. M. Chervin, and R. L. Jenne, 1988: Global distribution of total cloud cover and cloud type amounts over the ocean. U.S. Department of Energy DOE/ER-0406, 212 pp.

Weinreb, M. P., and M. L. Hill, 1980: Calculations of atmospheric radiances and brightness temperatures in infrared window channels of satellite radiometers. NOAA Tech. Rep. NESS 80, U. S. Dept. of Commerce, 40 pp. [Available from 5200 Auth Rd., Rm. 703, Camp Springs, MD 20746.]

Welch, R. M., S. K. Sengupta, and I. S. Kuo, 1988: Marine stratocumulus cloud fields off the coast of Southern California observed using LANDSAT imager. Part II: Textural analysis. *J. Appl. Meteor.*, **27,** 363–378.

Wielicki, B. A., and L. Parker, 1992: On the determination of cloud cover from satellite sensors: The effect of sensor spatial resolution. *J. Geophys. Res,* **97,** 12 799–12 823.

Wylie, D. P., W. P. Menzel, H. M. Woolf, and K. I. Strabala, 1994: Four years of global cirrus cloud statistics using HIRS. *J. Climate*, **7,** 1972–1986.

Yamanouchi, T., and S. Kawaguci, 1989: Cloud distribution in the Antarctic from AVHRR data of NOAA satellites and radiation measurements at the ground surface. *Proc. IAMAP 89 Scientific Assembly*, Vol. 2, Reading, United Kingdom, University of Reading, p. 17.